RESEARCH ARTICLE

Key Points:
- In a realistic model, remote baroclinic tides reduce subtidal shelf stratification by up to 50% compared to simulations without tides
- The increase in vertical mixing due to remote baroclinic tides increases the width of the inner shelf region
- Modifications to shelf stratification with tides are comparable to the observed seasonal cycle of stratification

Correspondence to:
S. Suanda,
ssuanda@ucsd.edu

The Effect of Barotropic and Baroclinic Tides on Coastal Stratification and Mixing

S. H. Suanda[1] (ID), **F. Feddersen[1]** (ID), and **N. Kumar[2]** (ID)

[1]Integrative Oceanography Division, Scripps Institution of Oceanography, La Jolla, CA, USA, [2]Civil and Environmental Engineering, University of Washington, Seattle, WA, USA

Abstract The effects of barotropic and baroclinic tides on subtidal stratification and vertical mixing are examined with high-resolution, three-dimensional numerical simulations of the Central Californian coastal upwelling region. A base simulation with realistic atmospheric and regional-scale boundary forcing but no tides (NT) is compared to two simulations with the addition of predominantly barotropic local tides (LT) and with combined barotropic and remotely generated, baroclinic tides (WT) with ≈ 100 W m^{-1} onshore baroclinic energy flux. During a 10 day period of coastal upwelling when the domain volume-averaged temperature is similar in all three simulations, LT has little difference in subtidal temperature and stratification compared to NT. In contrast, the addition of remote baroclinic tides (WT) reduces the subtidal continental shelf stratification up to 50% relative to NT. Idealized simulations to isolate barotropic and baroclinic effects demonstrate that within a parameter space of typical U.S. West Coast continental shelf slopes, barotropic tidal currents, incident energy flux, and subtidal stratification, the dissipating baroclinic tide destroys stratification an order of magnitude faster than barotropic tides. In WT, the modeled vertical temperature diffusivity at the top (base) of the bottom (surface) boundary layer is increased up to 20 times relative to NT. Therefore, the width of the inner-shelf (region of surface and bottom boundary layer overlap) is increased approximately 4 times relative to NT. The change in stratification due to dissipating baroclinic tides is comparable to the magnitude of the observed seasonal cycle of stratification.

1. Introduction

On the continental shelf (from the shoreline to ≈ 150 m water depth), water temperature and stratification are important factors that determine the vertical distribution of water column properties, cross-shelf circulation, and the efficiency of air-sea exchange. For classic two-dimensional wind-driven coastal upwelling, the continental shelf has different dynamical regimes based on the distribution of vertical mixing and coastal stratification (e.g., Lentz & Fewings, 2012). On the outer and midshelf, turbulent surface and bottom boundary layers are separated by a quasi-inviscid, stratified interior. On the inner shelf, turbulent boundary layers overlap and stratification is weak (e.g., Austin & Lentz, 2002; Lentz, 1995, 2001; Lentz & Fewings, 2012).

Continental shelf turbulence levels and boundary layer thickness are also affected by other processes, such as barotropic (surface) and baroclinic (internal) tides. Barotropic tides are forced directly by lunar and solar gravitational effects, and are damped by interactions with bathymetry through the generation of baroclinic tides and bottom boundary layer dissipation (e.g., Egbert & Ray, 2001; Garrett & Kunze, 2007). Barotopic tides have mostly depth-uniform currents and small temperature oscillations. Through nonlinear and dissipative effects, they can drive residual flows and induce vertical mixing on subtidal timescales. On the broad European shelf, barotropic tidal mixing generates seasonally varying, well-defined fronts with temperature gradients up to 1 °C km^{-1} (e.g., Simpson & Hunter, 1974). Barotropic tidal mixing also affects the vertical structure of coastal plumes both near and far from their source (e.g., Giddings et al., 2014; Liu et al., 2009). On the New England continental shelf, barotropic tidal currents up to 0.35 m s^{-1} and highly variable bathymetry, create a residual circulation comparable to wind-driven flow (Ganju et al., 2011; He & Wilkin, 2006; Kirincich et al., 2013). In this region, an injection of Fluorescein dye into an energetic barotropic tidally driven bottom boundary layer, was uniformly mixed through two-thirds of the entire water column (≈ 40 m in the vertical) within 24 h (Houghton & Ho, 2001). Tidal mixing can also influence wind-driven boundary layers. Idealized two-dimensional simulations with wind forcing and barotropic tides representative of the

mid-Atlantic Bight result in thicker bottom boundary layers and reduced inner-shelf stratification relative to wind-only simulations (Castelao et al., 2010).

Baroclinic tides have vertically sheared currents and potentially large temperature fluctuations. Approximately 30% of the global energy input into baroclinic tides is dissipated on continental margins, onshore of the toe of the continental slope (e.g., Waterhouse et al., 2014). A linear internal wave scattering model suggests that 10% of the energy input to baroclinic tides (≈ 0.1 TW) is transmitted and eventually dissipated on the continental shelf (Kelly et al., 2013a). On the continental shelf, observations indicate that midwater column turbulence is elevated with strong internal tide activity (e.g., MacKinnon & Gregg, 2003a).

Baroclinic tidal generation, propagation, and dissipation are often studied with regional numerical simulations of tides and varying wind forcing, and/or mesoscale variability (e.g., Buijsman et al., 2011; Carter, 2010; Holloway, 2001; Kerry et al., 2014; Kumar et al., 2015; Osborne et al., 2011, 2014). In these models, baroclinic tides are either generated within the domain by barotropic tidal flow interacting with near-critical bottom bathymetry (e.g., Ponte & Cornuelle, 2013), or enter the domain through prescribed lateral boundary conditions (e.g., Janekovic & Powell, 2012). These studies predominantly focus on tidal-band energetics, with limited discussion of the long-term, subtidal effect of simulating tides. Analogous to surface gravity waves approaching the shore, internal waves also break and vertically mix the water column over a region termed the "internal surfzone" (e.g., Huthnance, 1995; Thorpe, 1999) or "internal swashzone" (e.g., Walter et al., 2012).

Global (e.g., Arbic et al., 2010), and regional (Hermann et al., 2002; Kartadikaria et al., 2011) models with tides show an increase in time-mean vertical mixing relative to those without tides. A two-dimensional model with baroclinic tides and coastal upwelling representative of the Oregon shelf (Kurapov et al., 2010), also report increased mixing and weaker bottom boundary layer stratification in internal tidal simulations. In this two-dimensional setting, baroclinic tides were generated at the shelf-break by an unrealistically large, cross-shore oriented barotropic tidal flow (0.2 m s^{-1}), necessary to create the target baroclinic tides. In the above studies, barotropic and baroclinic tidal effects were simultaneously present and it is unclear whether increased mixing was due to the barotropic or baroclinic tidal processes. In addition, how continental shelf characteristics determine the relative importance of barotropic and baroclinic tidal processes on subtidal vertical mixing is not understood.

Water temperature and stratification affect coastal ecosystems at a range of trophic levels (e.g., Cowen & Sponaugle, 2009; Tapia et al., 2009). For example, water temperature affects nutrient availability for primary production (e.g., McPhee-Shaw et al., 2007), and the recruitment and growth rate of coastal kelp and mussel species (e.g., Blanchette & Gaines, 2007). The output of regional numerical models, such as predicted water temperature, stratification and currents, are often used to assist in coastal management decisions. (e.g., Drake et al., 2011; Hinrichsen et al., 2011; Mitarai et al., 2009). Although regional operational models such as those from Integrated Ocean Observing Systems (https://ioos.noaa.gov/), well-represent wind-driven upwelling and mesoscale dynamics (e.g., Veneziani et al., 2009), they often do not include barotropic or baroclinic tides. Therefore, any potential effect of barotropic or baroclinic tides on tidal or subtidal vertical mixing and stratification is neglected. Regional models also have coarse horizontal resolution (e.g., 3 km resolution for the U.S. West Coast or Gulf of Mexico regions) relative to the width of some continental shelves. Observations from the "internal surfzone" suggest that within 5 km of the shoreline, baroclinic tidal characteristics are substantially transformed relative to offshore (e.g., Lerczak et al., 2003; Nam & Send, 2011; Suanda & Barth, 2015). Furthermore, continental shelf variations in stratification and mixing affect the cross-shelf distribution of intertidal invertebrate larvae (e.g., Morgan et al., 2009a; Queiroga & Blanton, 2004), which often remain within 10 km of the shoreline during the dispersal stage (e.g., Fisher et al., 2014; Morgan et al., 2009b). Thus, even if tidal forcing were included in regional models, baroclinic tidal dynamics and the potential effect on coastal ecosystems within the inner shelf would be insufficiently resolved.

Here, the effect of barotropic and baroclinic tides on subtidal stratification and vertical mixing is examined with three independent, realistic, and high-resolution three-dimensional simulations of the Central Californian continental shelf. A base simulation does not include barotropic or baroclinic tides. Two additional simulations have predominantly barotropic and combined barotropic and baroclinic tides. In addition, the independent impact of barotropic and baroclinic tides on vertical mixing and stratification are examined in highly idealized simulations with no other forcing. The setup of the models, comparison to observations, and analysis methods are described in section 2. The choice of an analysis period when the three realistic
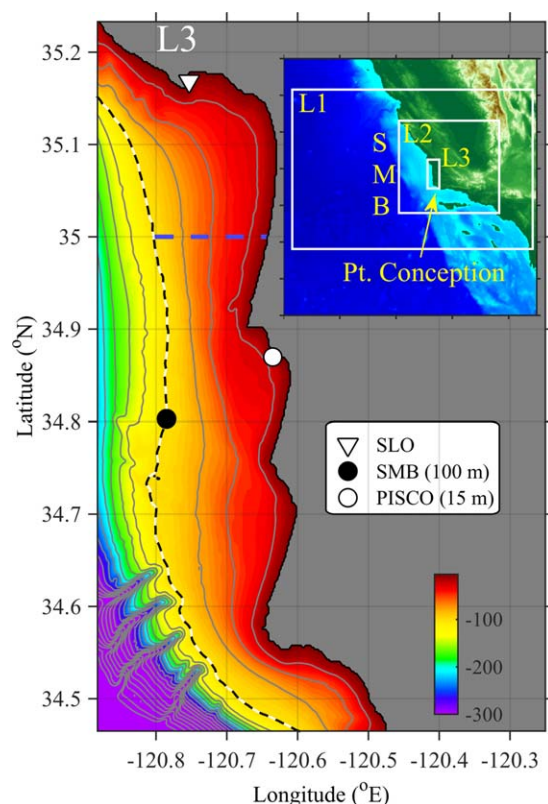
Figure 1. Map of the model region (**L3** domain) showing continental shelf bathymetry (gray lines are 25 m increments) and coastline adjacent to the Santa Maria Basin (SMB). The 100 m isobath is indicated by the black-white-dashed line. Dashed blue line marks the latitude of the cross-shore transects in Figures 7–9. Symbols denote the locations of the Port San Luis (SLO) tide gauge (white triangle), and the SMB (black circle, 100 m depth) and PISCO moorings (white circle, 15 m depth). Inset indicates the Central Californian study region. White outlines are domain boundaries for lower levels of nesting (large white rectangles, **L1** and **L2**) and for the NT, LT, and WT simulation domain (small white rectangle, **L3**).

simulations have similar volume-averaged temperature is described. A comparison of the three realistic simulations, contrasting the subtidal effect of barotropic and baroclinic tides are presented in section 3, with support from idealized model simulations. The implications of this study with reference to natural observed stratification variability and the width of the modeled inner shelf in this region are discussed in section 4. Section 5 provides a summary.

2. Methods

2.1. Santa Maria Basin Continental Shelf Simulations

2.1.1. Model Setup

The continental shelf adjacent to the Santa Maria Basin (SMB), north of Pt. Conception (Figure 1) is simulated with Rutgers ROMS (Regional Ocean Modeling System) with realistic surface forcing and boundary conditions for a 60 day period from 1 June to 31 July 2000. The SMB shelf is approximately 80 km long and 15 km wide from the shoreline to the 100 m isobath with bathymetric and coastline variability associated with multiple headlands and embayments (Figure 1). Some details of the ROMS setup and model-data comparison are described here with further information provided in Suanda et al. (2016). ROMS is a three-dimensional, terrain-following, open source numerical model that solves the Reynolds-averaged Navier-Stokes equations with hydrostatic and Boussinesq approximations (Haidvogel et al., 2008; Shchepetkin & McWilliams, 2005, 2009; Warner et al., 2010). For the SMB shelf, ROMS is configured with horizontal grid spacing of 200 m, 42 vertical levels, a horizontal eddy viscosity of 0.1 $m^2 s^{-1}$.

The k-ϵ model is used to represent the modeled temperature eddy diffusivity K_T (e.g., Warner et al., 2005). The k-ϵ submodel solves two transport equations for turbulent kinetic energy k, and turbulent dissipation rate ϵ, which are combined to give a turbulent length scale as a representation of subgrid vertical mixing (e.g., Burchard et al., 1998; Umlauf & Burchard, 2003). The source terms in these equations are functions of grid-resolved vertical gradients in horizontal velocity and density. Implementation of k-ϵ in ROMS is through a choice of stability function parameters (Warner et al., 2005). Broadly speaking, K_T increases with increased grid-resolved horizontal velocity shear and decreases with increased vertical density gradients. Previous work finds the k-ϵ model to perform well in a variety of coastal applications (e.g., Warner et al., 2005) including wind-driven coastal upwelling (e.g., Durski et al., 2004; Wijesekera et al., 2003).

ROMS is forced at the surface by daily-averaged atmospheric fields at 9 km resolution from the Coupled Ocean-Atmosphere Mesoscale Prediction System (COAMPS) model (Hodur et al., 2002). Radiation boundary conditions are applied to barotropic fields to allow outgoing energy (Chapman, 1985; Flather, 1976; Mason et al., 2010), and both radiation and nudging are used for baroclinic temperature and velocity boundary conditions (Marchesiello et al., 2001). Tracer and incoming baroclinic velocities are strongly nudged (with a 1 h time scale) and outgoing velocities are weakly nudged (365 d time scale).

The SMB shelf simulations (defined as grid **L3**, 200 m horizontal resolution) inherit boundary conditions from a series of one-way nested simulations on grids with larger domains and larger grid resolution (Figure 1, inset). The outermost simulation (**L0**) covers the entire northeastern Pacific ocean with 3 km horizontal resolution and uses climatological lateral boundary conditions from the World Ocean Atlas. This simulation reasonably reproduces the mean, seasonal, and mesoscale varying California Current System (Veneziani et al., 2009). A higher-resolution grid **L1** (1 km horizontal resolution, see inset of Figure 1) has boundary conditions inherited from the L0 solution. This nesting procedure is repeated for the second **L2** (600 m horizontal resolution, inset Figure 1) and third **L3** level of nesting. Both **L1** and **L2** use tracer and incoming velocity

nudging time scales of 6 h. To maintain consistency, all nested grids utilize the same COAMPS daily-averaged atmospheric forcing.

Three SMB simulations are run on grid **L3** and analyzed to study the effects of barotropic and baroclinic tides on stratification and mixing on the shelf with the same atmospheric forcing. The first simulation has no barotropic or baroclinic tides (no-tides, NT) and uses boundary conditions from the **L2** parent grid (Figure 1, inset) run without tides. A second simulation has barotropic tides only (local tides, LT) and uses the NT boundary conditions together with harmonic sea level and barotropic velocities of eight astronomical tidal constituents (K_2, S_2, M_2, N_2, K_1, P_1, O_1, Q_1) and two overtides (M_6, M_4) from the Tidal Constituent Database for the Eastern North Pacific Ocean (e.g., Mark et al., 2004). The database was constructed by forcing a depth-integrated, high coastal resolution, finite element hydrodynamic model (ADCIRC, Advanced Circulation) with the equilibrium tidal potential (e.g., Mark et al., 2004). This LT simulation has very weak baroclinic tides because most of the bathymetric slope within the **L3** grid is subcritical to baroclinic tidal generation (e.g., Holloway, 2001; Ponte & Cornuelle, 2013). Bathymetric slope criticality is defined relative to the slope of an internal wave characteristic in the (x, z) plane. For example, a semidiurnal internal wave with frequency ω_{M2} has a characteristic slope given by:

$$\frac{dz}{dx} = \left(\frac{\omega_{M2}^2 - f^2}{N_b^2 - \omega_{M2}^2}\right)^{-1/2},$$ (1)

where f is the Coriolis frequency and N_b is the near-bottom stratification. Given the mean N_b in the **L3** domain, the semidiurnal characteristic is nearly always 2–5 times steeper than the slope of the SMB shelf, particularly north of 34.65° (Figure 1). This indicates that an incident semidiurnal internal tide forward reflects toward the shoreline. The third simulation has both barotropic and baroclinic tides (with-tides, WT). This simulation inherits boundary conditions from the **L2** parent grid with the addition of the ADCIRC tidal forcing applied to the **L2** boundaries. Within the **L2** grid, there are many regions of barotropic-to-baroclinic tidal conversion which generate a time-average up to 0.05 W m^{-2} baroclinic tidal energy resulting in a net semidiurnal internal tide energy flux of ≈ 100 W m^{-1} at the **L3** boundary (N. Kumar, personal communication, 2017). These are designated as "remote" baroclinic tides as they propagate throughout **L2** and are transmitted to the higher-resolution **L3** domain via lateral boundary conditions. Baroclinic tides are simulated with a hydrostatic model to remain consistent with the models that supply the outer boundary conditions. Furthermore, horizontal grid spacing must be smaller than half the water depth to resolve nonydrostatic effects (Vitousek & Fringer, 2011). Over typical continental shelf depths ≈ 50 m, unrealistically small grid spacing would be needed to accurately capture these effects in a nonhydrostatic model.

2.1.2. SMB Simulations: Comparison to Observations

In the subtidal band (frequencies < 0.025 cph), the three SMB simulations compare favorably to moored observations over the 2 month period (Suanda et al., 2016). Here, a limited comparison to observations focuses on tidal-band and higher frequencies. The modeled barotropic tide is compared to observed sea level from the Port San Luis tide gauge (Figure 1, white triangle) via harmonic analysis using T_TIDE (Pawlowicz et al., 2002). Two of the largest semidiurnal (M_2, S_2) and diurnal (K_1 and O_1) tidal constituents are well reproduced by both LT and WT models to within 10% of the observed value (Figure 2a). The modeled N_2 constituent is within 20% of the observed amplitude with errors of 3 cm. All modeled tidal phases are within 2 h of observed, except for the modeled N_2 constituent that lags observations by 4 h (not shown). Sea level phase differences between LT and WT simulations were all less than 15 min, and similar to the ADCIRC tidal forcing. The similarity of the barotropic fields in LT and WT, suggest that model domain size has a small effect on barotropic tidal processes in this region similar to Southern California Bight and Monterey Bay results (Hall & Carter, 2010; Ponte & Cornuelle, 2013).

Baroclinic fields are compared to the SMB mooring deployed near the shelf edge on the 100 m isobath (Figure 1, black circle). Temperature spectra are calculated from observations at 25 and 45 m below the surface and subsequently averaged together (Figure 2b). Observed east-west velocity spectra are calculated from observations 5 m below the sea surface (Figure 2c). Modeled temperature and velocity spectra are similarly calculated for the SMB simulations (WT, LT, and NT). In the subtidal band, the modeled and observed temperature spectra (Figure 2b) and velocity spectra (Figure 2c) are similar. At tidal and higher-frequency bands (frequencies > 0.025 cph), the observed temperature and velocity spectra have peaks at diurnal, semidiurnal, and the twice semidiurnal harmonic (black curves in Figures 2b and 2c). At the SMB shelf latitude, the diurnal frequency is subinertial ($\omega_{K1} < f$). All three SMB simulations underrepresent the observed diurnal peak in the
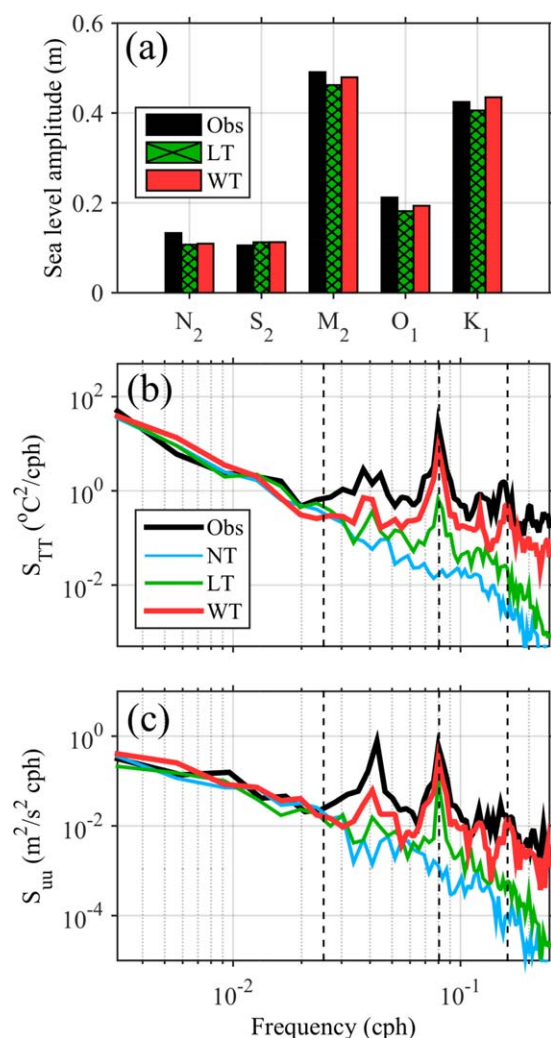
Figure 2. (a) Major semidiurnal (N_2, S_2, M_2) and diurnal (O_1, K_1) sea level tidal constituents at Port San Luis tide gauge for observed (black) and simulated with local tides (LT, hatched green) and total tides (WT, red). (b) Temperature spectra versus frequency from 25 to 45 m water depth at the SMB mooring location (see Figure 1) for observed (Obs, thick black) and simulated with no tides (NT, cyan), local tides (LT, green), and total tides (WT, thick red). Vertical-dashed lines are the subtidal cutoff (1/40 h, 0.025 cph), dominant semidiurnal (1/12.42 h, 0.0805 cph), and its first harmonic (1/6.21 h, 0.0161 cph). (c) East-west velocity spectra from 5 m water depth. Line colors and vertical-dashed lines are the same as Figure 2b.

temperature and velocity spectra, likely due to the lack of diurnal wind-forcing (sea-breeze), which has been shown to drive diurnal temperature and velocity variability on the SMB shelf (Cudaback & McPhee-Shaw, 2009; Pidgeon & Winant, 2005; Walter et al., 2017). Subinertial internal diurnal tidal motions can also be generated by abrupt topography (e.g., Beckenbach & Terrill, 2008). The waves are evanescent with decay scales potentially long relative to the model domain. The WT simulation has a stronger diurnal tidal response than LT (Figures 2b and 2c) because topographically generated diurnal internal motions in **L2** can also be transmitted to **L3**. The WT temperature and velocity spectra have semidiurnal and harmonic peaks similar to the observed (compare red and black curves in Figures 2b and 2c) in addition to elevated background levels. This indicates that WT baroclinic tidal energy is qualitatively similar to the observed. The LT simulation also has a semidiurnal peak in temperature and velocity, but an order of magnitude less than observed, and without the semidiurnal harmonic (green curves in Figures 2b and 2c). This demonstrates that baroclinic tides are significantly underproduced in LT. Through the tidal and high-frequency band, the NT temperature and velocity spectra are red with no pronounced peaks (blue curves in Figures 2b and 2c).

2.1.3. Analysis Period

To assess the role of tides in modifying the mean temperature distribution within the no tides (NT), local tides (LT), and with tides (WT) simulations, an analysis period is chosen when the volume-averaged temperature (heat content) within all simulations are equivalent. For each simulation, volume-averaged temperature $T_v(t)$ is defined as:

$$T_v(t) = \frac{\int_{L3} T(x,y,z,t)dV}{\int_{L3} dV}, \qquad (2)$$

where the volume integral is over the entire **L3** domain (200 m horizontal resolution). The cross-shore coordinate (x) is positive shoreward with the coastline at $x = 0$. The along-shore coordinate (y) is positive poleward and the vertical coordinate (z) is positive upward with time-mean sea level at $z = 0$. During the simulation period, wind forcing is predominantly from the northwest, favorable to coastal upwelling, except for relaxation and reversal periods (Figure 3a). In all simulations, T_v is correlated ($r \approx 0.4$) with the along-shelf component of the wind (Figure 3b). NT and LT simulations are similar, with a maximum absolute difference $T_v < 0.15°C$ for the entire 2 month simulation, thus indicating that local tidal processes do not strongly affect the total heat content during either upwelling or wind relaxation. The difference in T_v between NT and WT is similarly small during upwelling, but can reach 0.4°C follow-

ing periods of wind relaxation, when a poleward flow advects warm Santa Barbara Channel (SBC) water northward to the SMB shelf (Melton et al., 2009; Suanda et al., 2016; Washburn et al., 2011). The SBC water mass is different between NT and WT due to SBC mixing with the addition of tides at the **L2** grid boundaries. Once advected onto the SMB shelf, persistent differences in NT and WT T_v last about 1 week after winds return to upwelling-favorable. Given the difference in temperature advection, differences in temperature distribution within relaxation periods cannot be attributed solely to mixing processes. These periods are therefore avoided in the subsequent analysis.

During prolonged wind-driven upwelling, the average temperature T_v between SMB models is similar and indicates comparable heat content throughout the three model simulations. Temperature differences between NT, LT, and WT during this period indicate variations in the horizontal and vertical distribution of temperature within **L3**, and form the focus of this manuscript. Thus, the upwelling period between 3 and 13 July is chosen as the analysis period to compare the temperature distribution among the SMB simulations (blue shading, Figure 3).
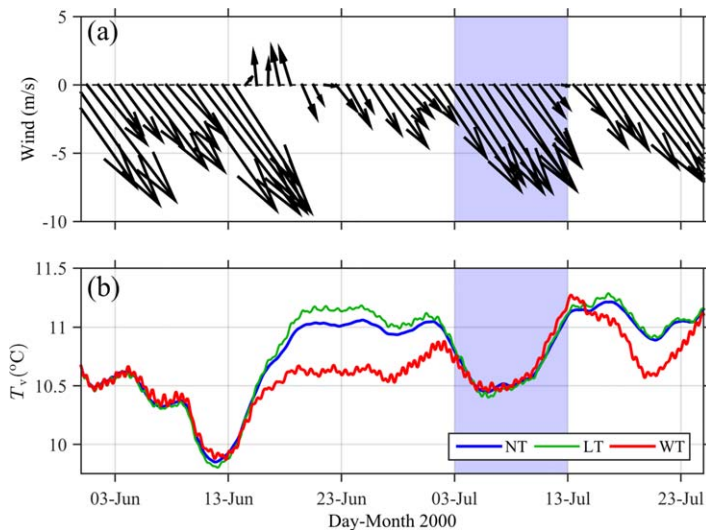
Figure 3. Two month time-series of (a) daily-averaged COAMPS vector winds representative of regional wind forcing. (b) Time series of model region volume-averaged temperature (T_v) for simulations with no tides (NT), local tides (LT), and total tides (WT). In both plots, the shaded blue region 3–13 July corresponds to the upwelling period analyzed in Results.

The analysis period begins with a weak upwelling-favorable wind on 3 July 2000 which increases in magnitude to moderate ($\approx 8\,\mathrm{m\ s^{-1}}$), and then decreases to near zero on 13 July 2000. The period also encompasses the transition from neap to spring tide and back toward neap (not shown). Model output from the NT, LT, and WT simulations are compared with 10 day time averages spanning the analysis period (blue shading, Figure 3). For example, analysis period mean temperature is denoted,

$$\overline{T}^{(n)} = \frac{1}{\tau} \int_{t_0}^{t_0+\tau} T(x,y,z,t)dt \tag{3}$$

where n refers to the NT, LT, or WT simulation, t_0 is the beginning of the analysis period and $\tau = 10$ days. Mean differences between simulations are calculated with reference to the NT simulation, such that $\Delta\overline{T}^{(n-NT)} = \overline{T}^{(n)} - \overline{T}^{(NT)}$, where n refers to the LT or WT simulation.

2.2. Idealized Model Setup

The effect of barotropic tides (denoted BT) and baroclinic tides (denoted BC) on temperature distribution is separately assessed with two idealized (ID) ROMS models configured to be analogous to the SMB shelf without alongshore variations, surface forcing, or subtidal boundary conditions. The ID simulations are thus two-dimensional (x, z) with periodic alongshore (y) boundary conditions and no wind or surface buoyancy forcing. The ID simulations have 30 vertical levels with increased resolution in the surface and bottom layers and are on an f-plane with Coriolis acceleration associated with latitude 35.0°N. An 85 km domain with uniform cross-shore grid spacing of 500 m is used with 10 grid points in y and 170 grid points in x. Offshore, the bathymetry is flat with a uniform depth of 300 m for 40 km, then rises with a uniform slope of 0.008, similar to the SMB continental shelf slope at 35.0°N (Figure 4a). At 10 m depth, the bathymetry is flat and a 7.5 km wide sponge layer that absorbs baroclinic fluctuations is placed over the final 15 grid points ending in a wall. Through this sponge region, horizontal eddy viscosity increases from an interior value of 1 m² s⁻¹ to a boundary value of 50 m² s⁻¹. The offshore end of the sponge region is denoted as the shoreline (x=0). The initial constant thermal stratification of 0.06 °C m⁻¹ is uniformly applied in x and z, equivalent to the depth average stratification from the SMB shelf NT simulation (Figure 4b). Salinity variations are neglected, thus the vertical temperature gradient controls the stratification as measured by the Brunt-Vaisala frequency $N = (g\alpha\partial T/\partial z)^{1/2}$, where the thermal expansion coefficient $\alpha = 2\times10^{-4}$ °C⁻¹ is assumed constant.

A single semidiurnal tidal constituent with period of 12.42 h (M_2) is applied as either barotropic or baroclinic forcing at the offshore boundary of the ID simulations. For the BT case, the offshore boundary condition of Flather-Chapman is specified with a cross-shore depth-uniform periodic flow $\overline{u} = U_o\cos(\omega_{M2}t)$, where ω_{M2} is the M_2 tidal radian frequency. Interior model dynamics solve for sea level (Chapman, 1985; Flather, 1976). Radiation boundary conditions are specified on depth-dependent u', v', and T'. In the BT case, the tidal forcing produces variability in sea level with almost 2 m amplitude. Although this sea level is approximately 4 times the amplitude of observed M_2 sea level, it is necessary to create a barotropic flow of magnitude consistent with those produced in the SMB shelf models, where the tide propagates alongshore as a Kelvin wave (e.g., Kurapov et al., 2010).

In the BC case, the offshore boundary condition is clamped to a baroclinic cross-shore flow u', along-shore flow v', and temperature perturbation T' consistent with a vertically standing mode-1 internal wave (Johnston & Merrifield, 2003). A constant baroclinic wave-averaged, depth-integrated energy flux of $EF^{M2} = 100\,\mathrm{W\ m^{-1}}$, approximately equivalent to the mean shoreward energy flux found in the WT model of this region, is applied at the boundary. Boundary conditions for
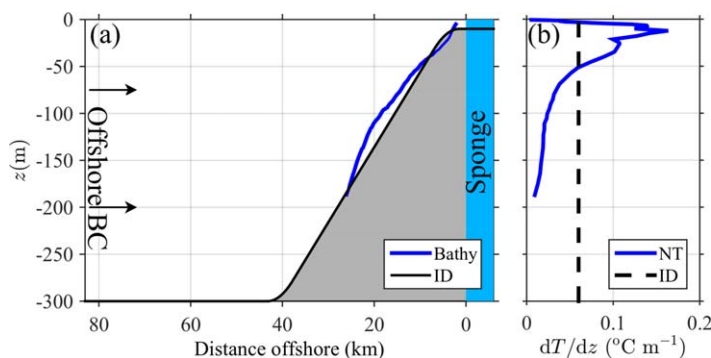

Figure 4. (a) Bathymetry versus distance offshore (x) from the idealized (ID) model (gray, black) and the realistic model region at 35.0°N latitude (see horizontal-dashed line, Figure 1). In ID model, shoreward of x = 0 a 7.5 km wide sponge layer covers the final 15 grid points of the domain. (b) Mean stratification $d\overline{T}/dz$ versus depth for the NT simulation (blue) and initial stratification used for ID model (dashed black).
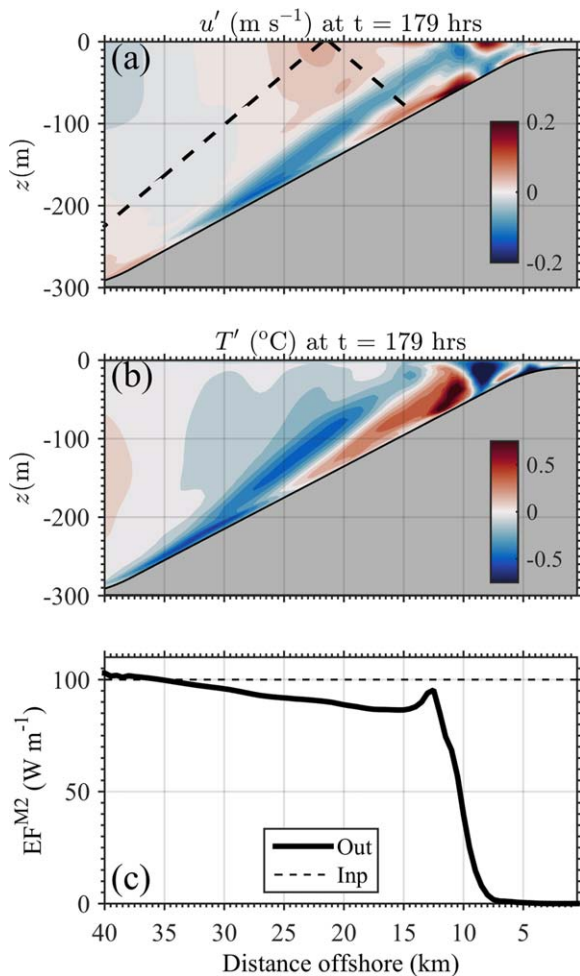
Figure 5. Idealized (ID) baroclinic model snapshots at $t = 179$ h of (a) perturbation cross-shore velocity u' and (b) perturbation temperature T' as a function of distance offshore (x) and z. Thick-dashed lines in Figure 5a represent the slope of a semidiurnal internal wave characteristic. (c) Wave-averaged, depth-integrated semidiurnal energy flux EF^{M2} versus distance offshore from ID baroclinic model. Dashed line indicates input $EF^{M2} = 100$ W m^{-1} applied at offshore boundary ($x = 85$ km).

baroclinic velocity u', v', and temperature T', are found from the polarization relation of a first-mode internal wave (see Appendix A). A BC model snapshot 179 h into simulation shows horizontal velocity and temperature perturbation fields consistent with a mode-1 baroclinic wave offshore of the slope (Figures 5a and 5b). Onshore of the slope, a portion of the mode-1 energy is transferred to higher vertical wave numbers, whose signature is a beam emanating from the bottom toward the surface (e.g., Johnston & Merrifield, 2003; Kelly et al., 2013b). For the initial stratification (N) and bathymetric slope of the SMB shelf, the internal wave characteristic is steeper than the bathymetric slope, and the wave forward-reflects toward shore (Figures 5a and 5b). This aspect is essential to the dynamics explored here (section 3.3). The internal wave beam continues upslope until nonlinear effects give rise to large values of velocity and perturbation temperature. Offshore of the slope, onshore internal wave energy flux is consistent with a mode-1 wave (Figure 5c). Wave-averaged energy flux slowly decreases over the first 27 km of the slope until approximately 80 m water depth (12 km from shore) where it quickly decreases toward zero nearshore. The hydrostatic ROMS model does not permit density overturns, potentially important in realistic internal wave breaking kinematics. Instead, the $k-\epsilon$ closure produces elevated eddy viscosity and diffusivity in this nearshore region to dissipate energy (section 3.3). Both ID simulations are run for 10 days, the same length as the analysis period in SMB simulations. A tidal-average is taken over the last day of simulation representative of the subtidal ending state. For example, in the temperature field:

$$T_e = \frac{1}{\tau_{ID}} \int_{t_9}^{t_9 + \tau_{ID}} T(x, z) dt \qquad (4)$$

where $t9$ is the 9th day of simulation and τ_{ID} is 24 h.

3. Results

3.1. Temperature Distribution

The analysis period average surface $\overline{\overline{T}}^{(NT)}$ (equation (3)) is consistent with regional coastal upwelling (Figure 6a). Offshore, in water depths greater than 100 m, relatively warm surface water $\approx 15.5\,°C$ stretches along the entire ≈ 100 km of coastline with little spatial variability except in the northern and southern parts of the domain. Onshore of 100 m depth, surface temperatures are up to 3 °C colder with the coldest surface $\overline{\overline{T}}^{(NT)}$ found in the downwind (southern) side of each headland, likely related to headland-intensified upwelling (e.g., Gan & Allen, 2002). The LT simulation surface $\overline{\overline{T}}^{(LT)}$ is similar to surface $\overline{\overline{T}}^{(NT)}$, with small $\Delta\overline{\overline{T}}^{(LT-NT)}$ spatial mean of $-0.01°C$, spatial root-mean-square (rms) of $0.06°C$, and no discernible spatial pattern (Figure 6b). In contrast, WT surface temperature $\overline{\overline{T}}^{(WT)}$ is much different, as $\Delta\overline{\overline{T}}^{(WT-NT)}$ has spatial mean $-0.14°C$ and spatial variability 5 times larger than $\Delta\overline{\overline{T}}^{(LT-NT)}$ with an rms of 0.33 °C (Figure 6c). Methods (section 2.1.3) demonstrate that the volume-averaged temperature T_V is similar between WT and NT during the analysis period. Thus, spatial mean surface $\Delta\overline{\overline{T}}^{(WT-NT)} < 0$ indicates that on average subsurface $\Delta\overline{\overline{T}}^{(WT-NT)} > 0$. This average vertical structure is further examined here.

Subsurface temperature is examined on a cross-shore depth transect at 35.0°N, from the shoreline to the 100 m isobath (Figure 7). In the no tides simulation, $\overline{\overline{T}}^{(NT)}(x, z)$ indicates structure consistent with coastal upwelling with upward and onshore tilted isotherms in the upper 40 m of the water column (Figure 7a). At depth, isotherms are tilted downward consistent with a poleward undercurrent due to the poleward pressure gradient force, a feature of continental shelf observations within the California Current system (e.g., Connolly et al., 2013; Fewings et al., 2015; Gan & Allen, 2002; Huyer et al., 1989).
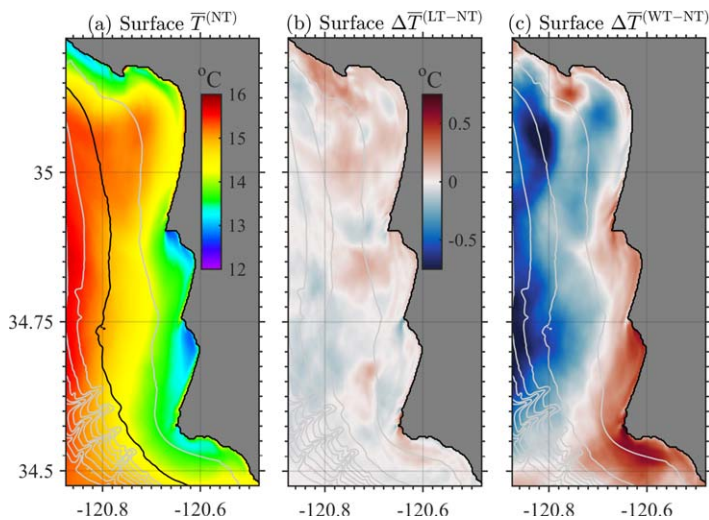
Figure 6. (a) Analysis period average (blue shading Figure 3) surface temperature from the NT simulation $\overline{T}^{(NT)}$ as a function of latitude and longitude. Analysis period average surface temperature difference between (b) LT and NT simulations $\Delta\overline{T}^{(LT-NT)}$ and (c) WT and NT simulations $\Delta\overline{T}^{(WT-NT)}$. In all plots, gray lines mark isobaths in 50 m increments and in Figure 6a the solid black line marks the 100 m isobath.

The LT average $\overline{T}^{(LT)}(x,z)$ is very similar to NT with a spatial rms ($\Delta\overline{T}^{(LT-NT)}$)=0.04 °C and no clear pattern (Figure 7b). A cross section of $\Delta\overline{T}^{(WT-NT)}$ has more significant temperature differences between simulations with spatial rms 0.25°C (Figure 7c). The largest $\Delta\overline{T}^{(WT-NT)}$ values are about 0.4°C found at 70 m water depth. Except for the small amount of bottom cooling offshore near the 100 m isobath, the spatial pattern of $\Delta\overline{T}^{(WT-NT)}$ is consistent across the shelf. Relative to NT, the mean water temperature has cooled by about 0.25°C in the near-surface at water depths shallower than 20 m and warmed by approximately the same amount at depth. Both the spatial (x, z) mean $\Delta\overline{T}^{(LT-NT)}$ and $\Delta\overline{T}^{(WT-NT)}$ are small (0.02 °C), again consistent with similar T_V for all simulations during the analysis period.

Three-dimensional effects are also evident, for example the spatial mean surface $\overline{T}^{(WT)}$ is $\approx 0.5\,°C$ warmer than surface $\overline{T}^{(NT)}$ downwind of all headlands (Figure 6c). As the same wind field is applied to the NT, LT, and WT simulations, headland-intensified upwelling (e.g., Gan & Allen, 2002; Roughan et al., 2005; Winant, 2006) is an important process in all SMB simulations. Relative to NT, headland-intensified upwelling in the WT simulation delivers relatively warmed subsurface water (Figure 7c) to the downwind side of the headlands.

3.2. Temperature Stratification and Diffusivity

To indicate the strength of mean model vertical mixing, the comparison of NT, LT, and WT temperature distributions are supplemented with cross-shore versus depth transects of analysis period average temperature stratification $d\overline{T}/dz(x,z)$ and thermal diffusivity $\overline{K}_T(x,z)$. Although K_T and dT/dz vary on subtidal and tidal timescales, here only analysis period averages are considered to focus on the long-term changes induced by barotropic and baroclinic tides.

Inshore (total water depth < 70 m), mean NT thermal stratification $d\overline{T}/dz^{(NT)}(x,z)$ at 35.0°N reaches a maximum of 0.5°C m^{-1} at approximately 10 m depth (Figure 8a). Although the lower water column is weakly stratified, high stratification in this nearshore thermocline contributes to a high spatial mean of $d\overline{T}/dz^{(NT)}$ of 0.09°C m^{-1}. Regions of high vertical mixing are predominantly found in distinct surface and bottom boundary layers (roughly, $\overline{K}_T \geq 10^{-4}$ m^2 s^{-1}) where $\overline{K}_T^{(NT)}$ can exceed 10^{-2} m^2 s^{-1} (Figure 8b). Without tides, modeled NT surface turbulence during the analysis period is predominantly driven by the wind, and bottom turbulence is generated by near-bed shear of the subtidal flow. The distance between the surface and bottom boundary layers decreases toward shallow water but remain well-separated by a quasi-inviscid interior ($\overline{K}_T < 10^{-4}$ m^2 s^{-1}) until the 7 m isobath (blue line, Figure 8b). Onshore of this point, $\overline{K}_T \geq 10^{-4}$ m^2 s^{-1} throughout the water column indicating that boundary layers overlap, and thereby defining the inner shelf (e.g., Austin & Lentz, 2002; Lentz & Fewings, 2012).

In LT, the overall picture is similar to NT including the magnitude and structure of the nearshore thermocline (Figure 8c). The main differences are found in slightly patchier levels of elevated $\overline{K}_T$ near the bottom boundary layer, and slightly increased $\overline{K}_T$ nearshore (Figure 8d). In contrast, $d\overline{T}/dz^{(WT)}$ and $\overline{K}_T^{(WT)}$ have larger differences compared to NT (Figures 8e and 8f). In WT, the strength of the inshore thermocline (where $d\overline{T}/dz^{(WT)}$ is maximum in total water depth < 70 m) is reduced to approximately half of $d\overline{T}/dz^{(NT)}$ with a maximum $d\overline{T}/dz^{(WT)}$ value of 0.25°C m^{-1} (Figure 8e). Vertical mixing is stronger in WT than both NT and LT, with regions of high $\overline{K}_T$ extending from the boundary layers to fill the middle of the water column (Figure 8f). The distance between the surface and bottom boundary layers is decreased in WT relative to NT such that the region where ($\overline{K}_T < 10^{-4}$ m^2 s^{-1}) terminates at 23 m isobath (blue line, Figure 8f). The implication of these results is further discussed in section 4.2 below.

Differences in $d\overline{T}/dz$ and $\overline{K}_T$ between simulations further illuminate these features (Figure 9). Between LT and NT, the average difference $\Delta d\overline{T}/dz^{(LT-NT)}$ is small, with the LT simulation overall -0.001°C m^{-1} less stratified than NT (Figure 9a). Moderate spatial variability is evident as the spatial rms difference of $\Delta d\overline{T}/dz^{(LT-NT)}$ is 0.01°C m^{-1}, including increased stratification at the base of the surface layer in the LT simulation. Some differences between $\overline{K}_T^{(LT)}$ and $\overline{K}_T^{(NT)}$ are visible as variable patches of the diffusivity ratio within
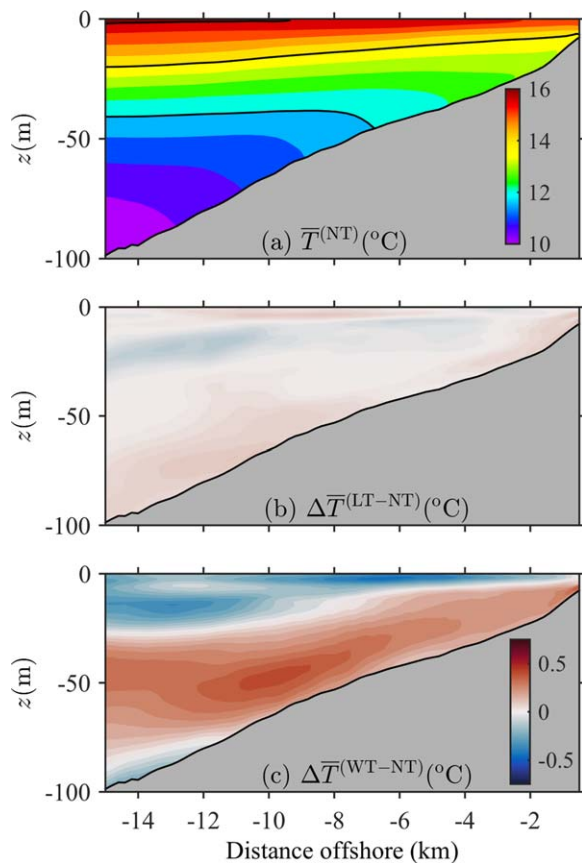
Figure 7. Analysis period averages on a cross-shore and depth transect (x, z) at latitude 35.0°N (see horizontal-dashed line, Figure 1): (a) average NT temperature $\overline{T}^{(NT)}$ with isotherms contour lines in 2°C increments (black). (b) Average temperature difference between LT and NT simulations $\Delta \overline{T}^{(LT-NT)}$. (c) Average temperature difference between the WT and NT simulations $\Delta \overline{T}^{(WT-NT)}$. Color bar in Figure 7c also applies to Figure 7b.

10 m of the bottom (Figure 9b). The greatest increase in $\overline{K}_T$ between NT and LT is a factor of 6 increase, less than an order of magnitude.

Larger differences are found between WT and NT. The sum total difference in mean stratification $\Delta d\overline{T}/dz^{(WT-NT)}$ is an order of magnitude larger than LT and NT at -0.1°C m^{-1} (Figure 9c). Most of the water column experiences this reduction in stratification, although reduced stratification is pronounced within the nearshore thermocline. Near the bed, the water column is actually more stratified in WT compared to NT. Larger differences are also found between $\overline{K}_T^{(WT)}$ and $\overline{K}_T^{(NT)}$ (Figure 9d). Up to a factor of 20 increase in $\overline{K}_T$ is found in the middle of the water column extending across the shelf from the 80 m isobath toward shore. There are also increases in $\overline{K}_T^{(WT)}$ relative to $\overline{K}_T^{(NT)}$ near the surface. However, at the surface and nearest to the bed, differences with NT are small and in fact decreases in near-bed diffusivity are found where the WT model is more stratified. In the three-dimensional SMB simulations, differences between $\overline{K}_T^{(WT)}$ or $\overline{K}_T^{(LT)}$ and $\overline{K}_T^{(NT)}$ near the sea bed (within ≈ 10 m) and the sea surface (within ≈ 5 m) are small, and indicate that turbulence near these boundaries in the NT simulation is not substantially modified by the addition of either barotropic or baroclinic tides (Figures 9b and 9d). In this case, near-boundary turbulence must be dominated by shear production due to processes in the NT simulation, also present in LT and WT simulations, such as wind-driven surface layer and low-frequency geostrophic flow.

3.3. Idealized Barotropic and Baroclinic Models

The large differences in stratification and vertical eddy diffusivity between the WT and NT simulations (Figures 9a and 9c) and the analogous small differences between the LT and NT simulations (Figures 9b and 9d) suggest that the enhanced mixing of the dissipating baroclinic tides significantly modifies the mean temperature and stratification distribution on the shelf. However, many baroclinic and barotropic tidal constituents are present in the WT simulation and all three SMB simulations have complex, three-dimensional coastal circulation with surface and large-scale boundary forcing. Thus, the precise mechanism reducing stratification is uncertain. The barotropic and baroclinic tidal effects in enhancing vertical mixing and reducing stratification are isolated with two idealized simulations with single-constituent barotropic (BT) and baroclinic (BC) tidal forcing only (section 2.2). The effect of barotropic and baroclinic tides is quantified with the difference of the tidally-averaged end temperature (equation (4)) from the constant stratification (Figure 4b) initial temperature $T_e - T_0$.

The ending temperature in the BT model $T_e^{(BT)}$ is similar to the initial temperature with small $|T_e^{(BT)} - T_0| < 0.2$ °C (Figure 10a). This implies that barotropic flow advects mean density across the slope, only slightly cools (warms) the surface (bottom) waters relative to initial temperature T_0, and weakly reduces stratification. At the end of the simulation, tidally-averaged BT model diffusivity is mostly weak except near-bed where a 10 m thick shear-driven bottom boundary layer is formed with $K_T^{(BT)} \geq 10^{-3}$ m^2 s^{-1}. In addition, at 12 km offshore a small patch of elevated $K_T^{(BT)}$ is detached from the boundary layer. These results are comparable to the small change in temperature $\Delta \overline{T}^{(LT-NT)}$ (Figure 7b) and weak increase in $\overline{K}_T^{(LT)}$ is found relative to $\overline{K}_T^{(NT)}$ (Figure 9b).

In the idealized BC simulation, the ending temperature $T_e^{(BC)}$ structure is much different with stronger cooling (warming) of surface (bottom) waters relative to initial temperature T_0 compared to $T_e^{(BT)}$ (Figure 10b). These results are qualitatively similar to $\Delta \overline{T}^{(WT-NT)}$. Although the temperature change here $|T_e^{(BC)} - T_0|$ is somewhat larger than $\Delta \overline{T}^{(WT-NT)}$, they are similarly concentrated in water depths shallower than 100 m (Figure 10c). In contrast to the enhanced BT turbulence confined near the bottom, the BC simulation has elevated $K_T^{(BC)}$ of 10^{-3} m^2 s^{-1} throughout much of the water column (Figure 10d).
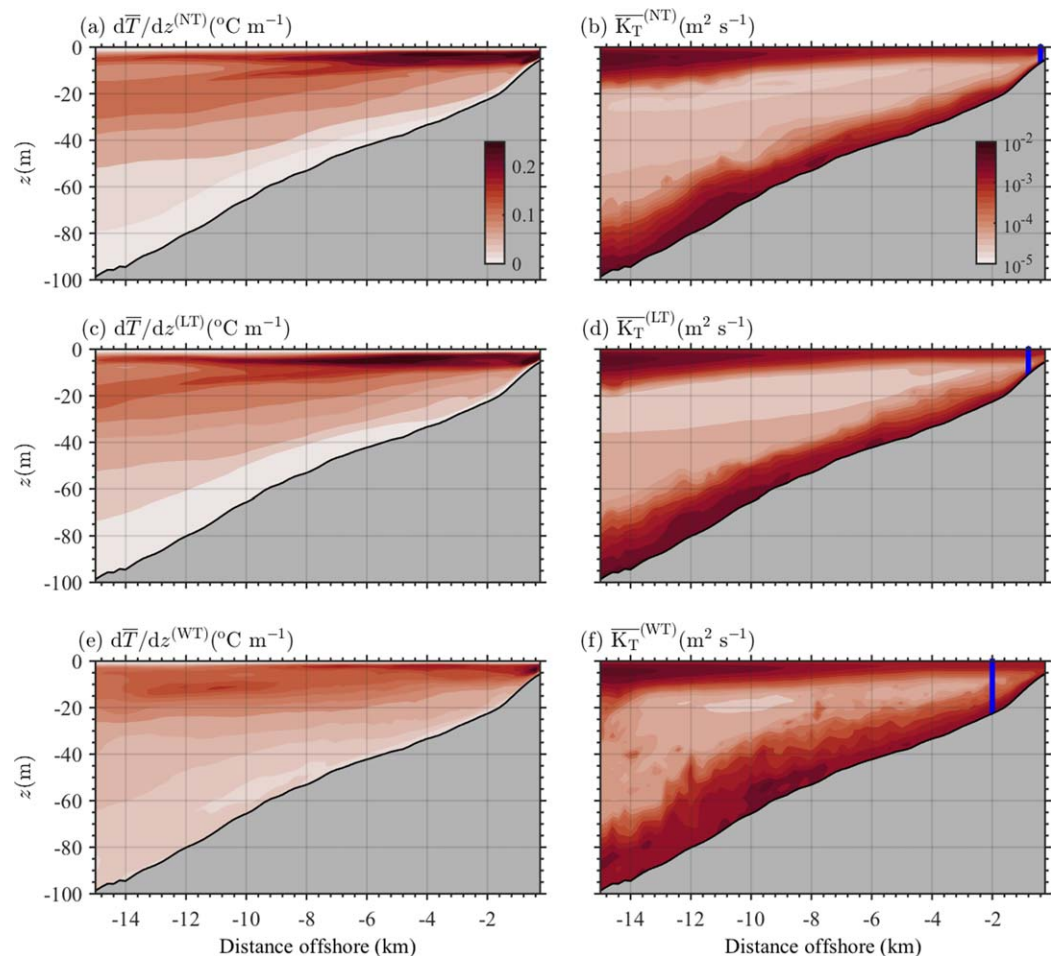
Figure 8. Analysis period averages on a cross-shore and depth transect (x, z) at latitude 35.0°N: (left: a, c, e) The vertical temperature gradient $d\overline{T}/dz$ (top to bottom, NT, LT, WT). (right: b, d, f) model-derived vertical temperature diffusivity $\overline{K_T}$ (top to bottom, NT, LT, WT). In right plots, blue line indicates the outer edge of the inner shelf defined as the region where surface and bottom boundary layers begin to overlap (see text section 3.2 and 4.2).

Temperature output between the 10 and 80 m isobaths from BT and BC models are used to estimate the rate of shelf stratification reduction in the idealized models due to separate barotropic and baroclinic tides. The BC rate (-2×10^{-3} °C m^{-1}d^{-1}) is approximately an order of magnitude faster than the BT rate (-3×10^{-4} °C m^{-1}d^{-1}). Although a similar analysis to separate baroclinic from barotropic tides cannot be done with the SMB simulations, an estimate is done by comparing typical values of $\Delta d\overline{T}/dz^{(LT-NT)}$ and $\Delta d\overline{T}/dz^{(WT-NT)}$ from their spatial root-mean-square (x, z) as above (section 3.2, Figures 9a and 9c). These result in rms ($\Delta d\overline{T}/dz^{(LT-NT)}$) = 0.01°C m^{-1} and rms ($\Delta d\overline{T}/dz^{(WT-NT)}$) = 0.03°C m^{-1}, respectively. Over the 10 day analysis period the WT rate is -3×10^{-3} °C m^{-1}d^{-1} and the LT rate is -1×10^{-3} °C m^{-1}d^{-1}, about 1/3 the rate of the WT reduction. Even with these simplifications, the results reaffirm the role of baroclinic tides in reducing mean stratification in both ID and SMB shelf simulations.

4. Discussion

4.1. Barotropic and Baroclinic Tidally-Induced Stratification Changes Relative to Natural Variability

Approximately 70% of the energy input to global baroclinic tides dissipates in the ocean interior, acting to maintain abyssal stratification that is important for the meridional overturning circulation (e.g., Munk & Wunsch, 1998; Waterhouse et al., 2014). About 10% of this power dissipates on the continental shelf (Kelly et al., 2013a). However, given that the coastal ocean accounts for approximately 10% of the total ocean
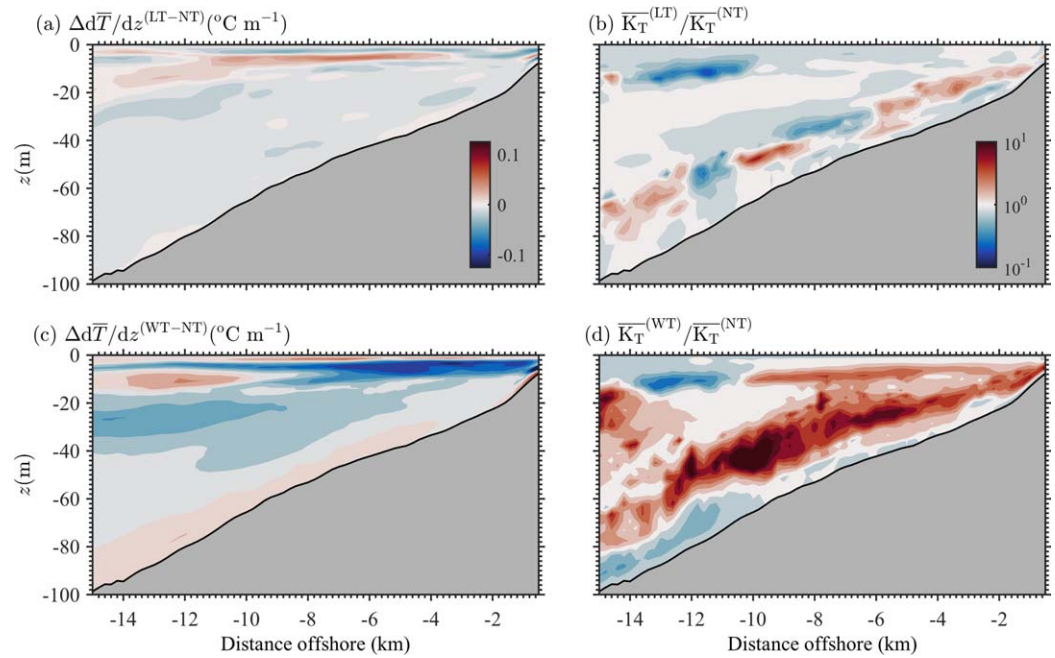
Figure 9. Analysis period average differences on a cross-shore and depth transect (x, z) at latitude 35.0°N. (left column: a, c) Temperature stratification difference between the (a) LT and NT $d\overline{T}/dz^{(LT-NT)}$, and (c) WT and NT $d\overline{T}/dz^{(WT-NT)}$ simulations. (right column: b, d) Mean vertical diffusivity $\overline{K}_T$ ratio between (b) LT and NT $\overline{K}_T^{(LT)}/\overline{K}_T^{(NT)}$, and (d) WT and NT $\overline{K}_T^{(WT)}/\overline{K}_T^{(NT)}$.

area and less than 1% of the total ocean volume, the effect of dissipating baroclinic tides is expected to be large on the continental shelf.

Here, the significance of barotropic and baroclinic tidal induced stratification changes ($\Delta d\overline{T}/dz^{(LT-NT)}$ and $\Delta d\overline{T}/dz^{(WT-NT)}$) are compared to the observed climatological seasonal cycle and variability of temperature
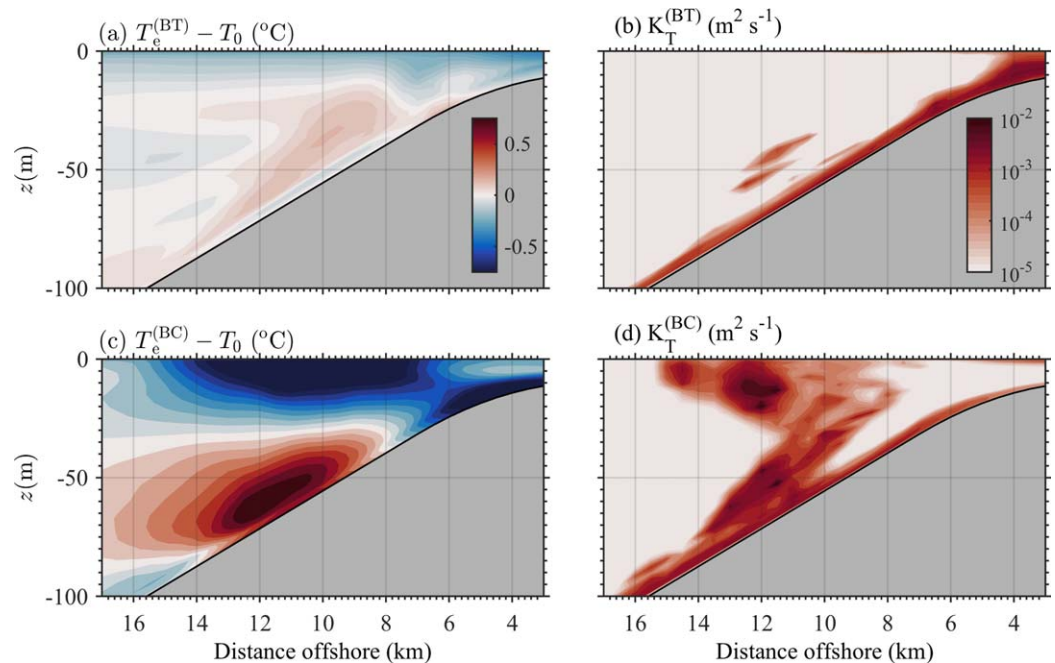

Figure 10. Idealized model (ID) results from (top) barotropic (BT) and (bottom) baroclinic (BC) simulations. (left: a, c) The tidally-averaged temperature after (a) 10 days of simulation $T_e^{(BT)}$ and (c) $T_e^{(BC)}$ less initial temperature T_0. (right: b, d) Tidally-averaged diffusivity K_T after 10 days of (b) barotropic and (c) baroclinic simulations.
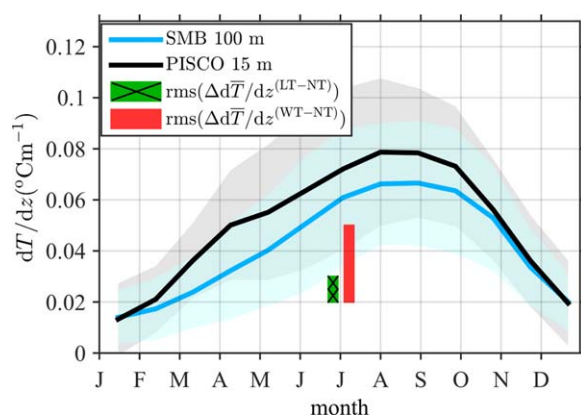
Figure 11. Climatological monthly-averaged vertical temperature gradient at the SMB mooring in 100 m water depth (*cyan*) and the PISCO mooring in 15 m water depth (black). For SMB (PISCO), solid lines are an average over 8 (16) years of observations, with shading as standard deviation (see Figure 1 for mooring locations). The height of the *hatched* green (*solid red*) line is the spatial root-mean-square temperature gradient difference between simulations LT-NT (WT-NT) at the 35.0°N cross-shore transect (Figure 9).

stratification at the SMB (100 m water depth) and PISCO (15 m water depth) moorings (black and white circles—Figure 1). The SMB mooring monthly stratification climatology is constructed over an 8 year period from 1994 to 2001 using the vertical temperature gradient from temperature measurements between 5 and 45 m depth. The PISCO stratification climatology is constructed over a 16 year period from 2000 to 2015 using the vertical temperature gradient from temperature measurements between 4 and 15 m depth. All temperature observations are subtidally filtered to remove baroclinic tidal fluctuations, then mean and standard deviations of temperature stratification are calculated for each calendar month (blue and black lines and shading in Figure 11). From the NT, LT, and WT simulations, a measure of shelf-wide $\Delta d\overline{T}/dz$ is calculated from spatial (x,z) root-mean-square as in section 3.2 and 3.3. The $\mathrm{rms}(\Delta d\overline{T}/dz^{(LT-NT)})$ and $\mathrm{rms}(\Delta d\overline{T}/dz^{(WT-NT)})$ are shown as green and red vertical lines (Figure 11).

The shape and strength of the seasonal cycle at both SMB and PISCO moorings are similar. Temperature stratification is weak (< 0.02°C m^{-1}) in the winter months of January and February, rising slowly through spring to reach a maximum of 0.065°C m^{-1} (0.08°C m^{-1}) at SMB (PISCO) during the late summer, and quickly declining in Fall to their annual minimum value (e.g., Cudaback et al., 2005). The standard deviation of the monthly means (shading, Figure 11) is roughly 0.02 °C m^{-1} at both locations and largest during the summer upwelling season (about 0.03°C m^{-1}). Adding barotropic tides (LT) has a relatively small effect on model subtidal stratification with $\mathrm{rms}(\Delta d\overline{T}/dz^{(LT-NT)}) = 0.01$ °C m^{-1} (Figure 11). In contrast, the effect of both barotropic and baroclinic tides (WT) induces subtidal stratification differences with $\mathrm{rms}(\Delta d\overline{T}/dz^{(WT-NT)}) = 0.03$ °C m^{-1} that are as large as the monthly mean variability, and almost as large as the seasonal cycle of stratification. Thus, to achieve seasonally varying realistic stratification, coastal simulations must consider the effect of barotropic and baroclinic tides. Furthermore, these results suggest that tidal considerations are important in all shelf regions with a remotely incident baroclinic tide.

4.2. Barotropic and Baroclinic Tidal Effects on the Width of the Inner Shelf

The inner shelf has been dynamically defined as the region where subtidal turbulent surface and bottom boundary layers overlap (e.g., Lentz & Fewings, 2012). In a realistic numerical model, a diagnostic of whether a region is on the inner shelf can have implications for coastal biology. On the inner shelf, vertical mixing of momentum and tracers, such as nutrients or planktonic larvae, between the surface and bottom is more efficient compared to the midshelf (Lentz & Fewings, 2012). Unlike on the mid and outer shelf, the along-shelf wind is not the primary driver of subtidal cross-shelf exchange in this region, and other processes such as cross-shelf winds (e.g., Fewings et al., 2008), along-shore convergences (e.g., Tilburg & Garvine, 2003), and surface gravity waves (e.g., Lentz et al., 2008) are more relevant. Previous studies have found that organism larvae on the inner shelf are more likely to remain in the nearshore during periods of upwelling-favorable wind forcing (Morgan et al., 2009b). An estimate of combined surface and bottom boundary layer thickness from regional observations finds the 15 m isobath to be dynamically on the inner shelf >50% of the time on the SMB shelf (Fewings et al., 2015). Delineating the outer edge of the inner shelf in a realistic stratified coastal simulation is useful to understand what cross-shelf exchange mechanisms are important at variable water depths or distances from shore.

The addition of barotropic and baroclinic tides significantly affects the location of the outer edge of the inner shelf. To apply the concept of surface and bottom boundary layer overlap, the inner shelf is defined within all simulations to be the offshore location where the entire water column is fully turbulent ($\overline{K_T} \geq 10^{-4}$ m^2 s^{-1}, see blue lines in Figures 8b, 8d, and 8f). For the NT simulation, over the analysis period the inner-shelf is about 0.4 km wide and extends to the 7 m isobath (blue line, Figure 8b). For the LT simulation, the inner-shelf width extends slightly deeper to the 11 m isobath located about 1 km from the shoreline (blue line, Figure 8d). In contrast, for WT the inner-shelf width extends to the 23 m isobath, 2 km from shore (blue line, Figure 8f). Only the outer edge of the WT inner shelf extends past the 15 m isobath, much
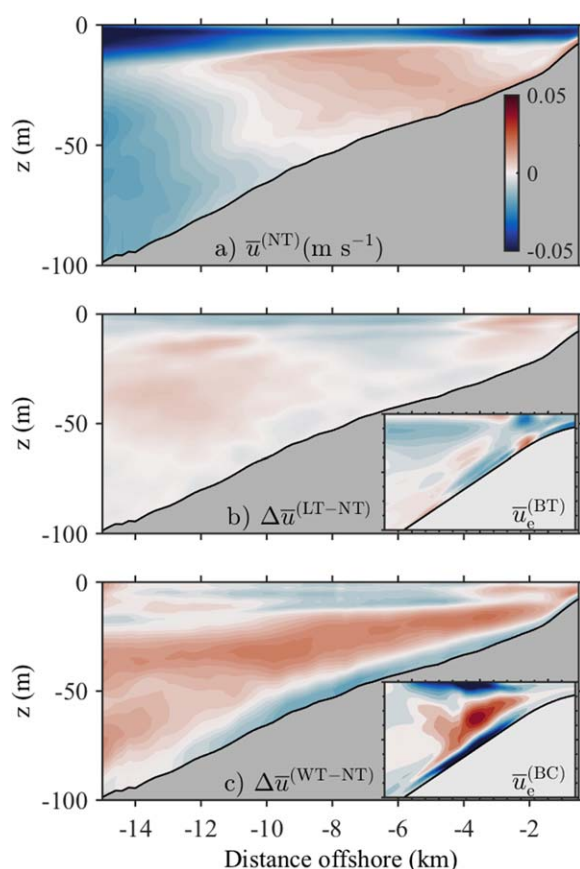
Figure 12. Analysis period average cross-shore and depth transect (x, z) at latitude 35.0°N. (a) Average NT east-west flow $(\overline{u})$. (b) East-west flow difference between the LT and NT simulation. (c) East-west flow difference between the WT and NT simulation. Inset in Figures 12b and 12c are tidally-averaged cross-shelf flow from idealized (b) BT and (c) BC simulations. Inset axis limits (x, z) are the same as Figure 10.

deeper than either NT or LT. In addition, over the analysis period the inner shelf in WT is 4 times wider than the NT inner shelf with the same subtidal atmospheric forcing conditions.

4.3. Barotropic and Baroclinic Tidal Residual Cross-Shore Circulation

The addition of barotropic and baroclinic tides modifies modeled shelf subtidal temperature, stratification, and vertical mixing. In addition, subtidal currents are potentially affected through the generation of residual flows. The analysis period average east-west velocity $\overline{u}$ is examined for differences in flow structure in the approximate cross-shore direction with the addition of barotropic and baroclinic tides (Figure 12). Analysis period mean $\overline{u}^{(NT)}$ shows strong offshore flow in the upper 10 m of the water column, consistent with Ekman transport due to upwelling favorable wind forcing (Figure 12a). Below this layer, a weak onshore return flow spans the remaining water column in water depth <70 m. Three-dimensional effects are also apparent as offshore of 70 m water depth, flow is weakly offshore throughout the water column. Differences between LT and NT $\Delta\overline{u}^{(LT-NT)}$ are minimal with weak variability (Figure 12b). The ending tidally-averaged cross-shore flow in the idealized barotropic tide simulation $(\overline{u}_e^{(BT)})$ is also weak (rms ≈ 0.01 m s^{-1}) although with a pattern of nearshore surface divergence balanced by a convergence at depth.

Differences between WT and NT $\Delta\overline{u}^{(WT-NT)}$ have rms ≈ 0.01 m s^{-1}, half of rms$(\overline{u}^{(NT)})$ and result in a distinct three-layer structure (Figure 12c). The offshore surface layer transport in WT is increased relative to NT, the midwater column has increased onshore flow, while the bottom has a net offshore flow in WT (Figure 12c). This structure is qualitatively consistent to the observed ending tidally-averaged cross-shore flow $(\overline{u}_e^{(BC)})$ in the idealized baroclinic tide simulation (see inset Figure 12c). As the idealized model has no other forcing, this structure suggests a mean cross-shore circulation driven by dissipating baroclinic tides. The three-layer structure also resembles the observed time-mean cross-shelf velocity profile in 15 m water depth at this location (Fewings et al., 2015). Fewings et al. (2015) interpret the vertical profile as being forced by a combination of wind and pressure gradient forcing. Dissipating baroclinic tides serve as an alternate explanation for the three-layer structure of the observed mean cross-shore flow profile, particularly during summer.

4.4. Comparison to Other Studies

Relative to NT, midwater column shelf stratification decreases with the addition of baroclinic (WT), and not barotropic tides (LT). The importance of remotely shoaling baroclinic tides on increasing mixing, potentially contrasts with results from the U.S. East Coast, which generally has a much gentler slope than the SMB shelf. An idealized modeling study found substantial changes to stratification and wind-driven circulation between 5 and 20 m water depth with the addition of barotropic, not baroclinic tides (Castelao et al., 2010). In Castelao et al. (2010), stratification and wind forcing were similar to the SMB conditions. However, barotropic tidal currents are weaker on the narrow U.S. West Coast shelf (Battisti & Clarke, 1982). The Castelao et al. (2010) study used tidal currents between 0.13 and 0.26 m s^{-1}, almost 3 times as strong as SMB shelf tidal currents. Castelao et al. (2010) did not include an incident baroclinic tide and, with subcritical bathymetry, did not have any baroclinic tide generation within the domain. With similar values of mean stratification, a subcritical semidiurnal internal tide on the SMB shelf is also subcritical on the more gently sloped East Coast shelf. In addition, baroclinic tidal energy flux can be significant on the U.S. East Coast relative to the SMB shelf. For example, shoreward semidiurnal baroclinic energy fluxes on the New England continental shelf are comparable to the SMB shelf in similar water depths (MacKinnon & Gregg, 2003b). However, with the same incident semidiurnal energy flux, energy dissipates over a shorter distance on a steep relative to a

gentle slope. This implies that the baroclinic tidal effects on stratification and mixing are stronger on steep, yet still subcritical, continental shelves.

5. Summary

The effects of barotropic and baroclinic tides on subtidal stratification and vertical mixing are examined with high-resolution, three-dimensional ROMS numerical simulations of the Central Californian continental shelf (from the shoreline to ≈ 150 m water depth) adjacent to the Santa Maria Basin (SMB). A base simulation with realistic atmospheric and regional-scale boundary forcing but no tides (NT) is compared to two simulations with the addition of predominantly barotropic local tides (LT) and with combined barotropic and remotely generated, baroclinic tides (WT) with ≈ 100 W m^{-1} onshore baroclinic energy flux. Both LT and WT simulations reproduce barotropic tidal elevations within 10% of tide gauge observations. Only the WT simulation produces semidiurnal and harmonic peaks as well as high-frequency (< 0.025 cph) energy levels similar to observations of midwater column temperature and near-surface velocity.

Over a 10 day period of persistent wind-driven coastal upwelling, the domain volume-averaged temperature is similar in all simulations. During this period, the LT simulation has little difference in subtidal temperature and stratification compared to NT. In contrast, the simulation with both barotropic and baroclinic tides (WT) is significantly different than NT as the upper 20 m has cooled by 0.25°C and warmed by a similar amount at depth. The WT vertical temperature redistribution amounts to a 50% reduction in subtidal stratification relative to NT. To isolate barotropic and baroclinic tidal effects on stratification, two idealized ROMS models are configured to be analogous to the SMB shelf without alongshore variations, surface or subtidal boundary forcing. The idealized models demonstrate that within a parameter space of typical U.S. West Coast shelf slopes, barotropic tidal currents, incident energy flux, and stratification, dissipating baroclinic tides reduce subtidal stratification an order of magnitude faster than the rate due to barotropic tides.

The addition of tides increases the strength of modeled midwater column subtidal vertical mixing. Differences between LT and NT are relatively small except for spatially intermittent increases in vertical temperature diffusivity across the shelf at the top of the bottom boundary layer. In WT, modeled vertical temperature diffusivity at the top (base) of the bottom (surface) boundary layer is increased up to 20 times relative to NT, thus extending turbulence through the midwater column. Therefore, the width of the inner shelf (region of boundary layer overlap) in WT extends 2 km from shore, approximately 4 times wider than the NT inner shelf. Only the WT simulation has an inner shelf that encompasses a water depth of 20 m, a more realistic extent compared to observational estimates.

The magnitude of reduced stratification in WT is comparable to monthly mean stratification variability and the magnitude of the observed seasonal cycle of stratification. The role of dissipating baroclinic tides on shelf stratification is potentially significant on continental shelves worldwide as 10% of the global energy input to baroclinic tides is dissipated on continental shelves with less than 1% of the world ocean volume.

Appendix A: Boundary Conditions for Idealized Baroclinic Tidal Simulation

Boundary conditions for the idealized baroclinic (BC) simulations include specification for state variables of horizontal flow, density, and sea level u, v, ρ, η at the boundary, for all depths and simulation time. The full horizontal flow u can consist of depth-dependent and depth-independent flow. In the BC case, no forcing is specified for the depth-independent flow or to sea level η, and the treatment of outgoing variability is left to the Flather-Chapman boundary condition as described in section 2.2 (Chapman, 1985; Flather, 1976).

In the idealized two-dimensional configuration, there is no variability in the along-shore coordinate y, and all other independent variables are specified at the offshore boundary ($x=L$). For constant stratification the vertical structure of first mode internal waves is given by $\cos(\pi z/h)$, where h is the water depth. For semidiurnal internal waves, temporal dependence in the direction of wave-propagation is given by $\cos(\omega_{M2} t)$ (Gill, 1982).

Including the effect of the earth's rotation, a description of a first baroclinic mode internal wave can be written:

$$[u', v', p'] = \left[1, \frac{\omega_{M2}}{f}, \rho_0 c \frac{(\omega_{M2}^2 - f^2)^{1/2}}{\omega_{M2}} \right] A \cos(\pi z/h) \cos(\omega_{M2} t) \tag{A1}$$

where u' is the velocity component in the direction of wave propagation, v' is perpendicular to wave propagation, and p' is the pressure perturbation associated with the wave. Here, A is the modal velocity amplitude, f the Coriolis frequency, ρ_0 a reference density 1025 kg m^{-3}, and c is the mode-1 internal wave speed,

$$c = \frac{Nh}{\pi}. \tag{A2}$$

Ignoring salinity effects, the Brunt-Vaisala frequency is related to a depth-uniform temperature gradient ($dT/dz = 0.06$°C m^{-1}), $N = (g\alpha \partial T/\partial z)^{1/2}$, with constant thermal expansion coefficient $\alpha = 2 \times 10^{-4}$ °C^{-1}. The initial background temperature profile is horizontally uniform and given by $T_0(z) = T_s + dT/dz(z)$, with surface temperature $T_s = 24$°C.

For linear waves, the modal velocity amplitude is related to the depth-integrated energy flux ($EF^{M2} = \int_{-h}^{0} \langle u'p' \rangle dz$) averaged over a semidiurnal wave period ($\langle . \rangle = 1/T_{M2} \int_0^{T_{M2}} . \, dt$), by:

$$\frac{A^2}{2} = \frac{EF^{M2} \omega_{M2}}{\rho_0 c (\omega_{M2}^2 - f^2)^{0.5} \int \cos(\pi z/h)^2 dz}. \tag{A3}$$

Internal wave temperature fluctuations are found from density fluctuations $T' = (\rho_0 - \rho')/\alpha$ related to the pressure perturbation through

$$\rho' = \frac{N^2}{g(N^2 - \omega_{M2}^2)} p'. \tag{A4}$$

Thus, with equation (A1), all variables are then prescribed at the boundaries:

$$u = A\cos(\pi z/h)\cos(\omega_{M2} t)$$

$$v = \frac{\omega_{M2}}{f} A\cos(\pi z/h)\cos(\omega_{M2} t)$$

$$T = T_0 + \left(\frac{\rho_0}{\alpha} - \frac{\rho_0 N^2 c(\omega_{M2}^2 - f^2)^{1/2}}{\alpha g(N^2 - \omega_{M2}^2)} A\cos(\pi z/h)\cos(\omega_{M2} t) \right). \tag{A5}$$

References

Arbic, B. K., Wallcraft, A. J., & Metzger, E. J. (2010). Concurrent simulation of the eddying general circulation and tides in a global ocean model. *Ocean Modelling*, *32*(3), 175–187. https://doi.org/10.1016/j.ocemod.2010.01.007

Austin, J. A., & Lentz, S. J. (2002). The inner shelf response to wind-driven upwelling and downwelling*. *Journal of Physical Oceanography*, *32*, 2171–2193.

Battisti, D. S., & Clarke, A. J. (1982). A simple method for estimating barotropic tidal currents on continental margins with specific application to the M2 tide off the Atlantic and Pacific coasts of the United States. *Journal of Physical Oceanography*, *12*(1), 8–16.

Beckenbach, E., & Terrill, E. (2008). Internal tides over abrupt topography in the Southern California Bight: Observations of diurnal waves poleward of the critical latitude. *Journal of Geophysical Research*, *113*, C02001. https://doi.org/10.1029/2006JC003905

Blanchette, C. A., & Gaines, S. D. (2007). Distribution, abundance, size and recruitment of the mussel, Mytilus californianus, across a major oceanographic and biogeographic boundary at Point Conception, California, USA. *Journal of Experimental Marine Biology and Ecology*, *340*(2), 268–279. https://doi.org/10.1016/j.jembe.2006.09.014

Buijsman, M. C., Uchiyama, Y., McWilliams, J. C., & Hill-Lindsay, C. R. (2011). Modeling semidiurnal internal tide variability in the Southern California Bight. *Journal of Physical Oceanography*, *42*(1), 62–77. https://doi.org/10.1175/2011JPO4597.1

Burchard, H., Petersen, O., & Rippeth, T. P. (1998). Comparing the performance of the Mellor-Yamada and the k-ϵ two-equation turbulence models. *Journal of Geophysical Research*, *103*(C5), 10543–10554. https://doi.org/10.1029/98JC00261

Carter, G. S. (2010). Barotropic and baroclinic M2 tides in the Monterey Bay Region. *Journal of Physical Oceanography*, *40*(8), 1766–1783. https://doi.org/10.1175/2010JPO4274.1

Castelao, R., Chant, R., Glenn, S., & Schofield, O. (2010). The effects of tides and oscillatory winds on the subtidal inner-shelf cross-shelf circulation. *Journal of Physical Oceanography*, *40*(4), 775–788. https://doi.org/10.1175/2009JPO4273.1

Chapman, D. C. (1985). Numerical treatment of cross-shelf open boundaries in a barotropic coastal ocean model. *Journal of Physical Oceanography*, *15*(6), 1060–1075. https://doi.org/10.1175/1520-0485(1985)015

Connolly, T. P., Hickey, B. M., Shulman, I., & Thomson, R. E. (2013). Coastal trapped waves, alongshore pressure gradients, and the California Undercurrent. *Journal of Physical Oceanography*, *44*(1), 319–342. https://doi.org/10.1175/JPO-D-13-095.1

Cowen, R. K., & Sponaugle, S. (2009). Larval dispersal and marine population connectivity. *Annual Review of Marine Science*, *1*, 443–466.

Cudaback, C. N., & McPhee-Shaw, E. (2009). Diurnal-period internal waves near point conception, California. *Estuarine, Coastal and Shelf Science*, *83*(3), 349–359. https://doi.org/10.1016/j.ecss.2008.12.018

Cudaback, C. N., Washburn, L., & Dever, E. (2005). Subtidal inner-shelf circulation near Point Conception, California. *Journal of Geophysical Research*, *110*, C10007. https://doi.org/10.1029/2004JC002608

Drake, P. T., Edwards, C. A., & Barth, J. A. (2011). Dispersion and connectivity estimates along the U.S. west coast from a realistic numerical model. *Journal of Marine Research*, *69*(1), 1–37. https://doi.org/10.1357/002224011798147615

Durski, S. M., Glenn, S. M., & Haidvogel, D. B. (2004). Vertical mixing schemes in the coastal ocean: Comparison of the level 2.5 Mellor-Yamada scheme with an enhanced version of the K profile parameterization. *Journal of Geophysical Research*, *109*, C01015. https://doi.org/10.1029/2002JC001702

Egbert, G. D., & Ray, R. D. (2001). Estimates of M2 tidal energy dissipation from TOPEX/Poseidon altimeter data. *Journal of Geophysical Research*, *106*(C10), 22475–22502. https://doi.org/10.1029/2000JC000699

Fewings, M., Lentz, S. J., & Fredericks, J. (2008). Observations of cross-shelf flow driven by cross-shelf winds on the inner continental shelf. *Journal of Physical Oceanography*, *38*, 2358–2378.

Fewings, M. R., Washburn, L., & Ohlmann, J. C. (2015). Coastal water circulation patterns around the Northern Channel Islands and Point Conception, California. *Progress in Oceanography*, *138*, 283–304. https://doi.org/10.1016/j.pocean.2015.10.001

Fisher, J. L., Peterson, W. T., & Morgan, S. G. (2014). Does larval advection explain latitudinal differences in recruitment across upwelling regimes? *Marine Ecology Progress Series*, *503*, 123–137.

Flather, R. (1976). A tidal model of the northwest European continental shelf. *Mémoires de la Société Royale des Sciences de Liège*, *10*(6), 141–164.

Gan, J., & Allen, J. S. (2002). A modeling study of shelf circulation off northern California in the region of the Coastal Ocean Dynamics Experiment: Response to relaxation of upwelling winds. *Journal of Geophysical Research*, *107*(C9), 3184.

Ganju, N. K., Lentz, S. J., Kirincich, A. R., & Farrar, J. T. (2011). Complex mean circulation over the inner shelf south of Martha's Vineyard revealed by observations and a high-resolution model. *Journal of Geophysical Research*, *116*, C10036. https://doi.org/10.1029/2011JC007035

Garrett, C., & Kunze, E. (2007). Internal tide generation in the deep ocean. *Annual Review of Fluid Mechanics*, *39*(1), 57–87. https://doi.org/10.1146/annurev.fluid.39.050905.110227

Giddings, S. N., MacCready, P., Hickey, B. M., Banas, N. S., Davis, K. A., Siedlecki, S. A., . . . Connolly, T. P. (2014). Hindcasts of potential harmful algal bloom transport pathways on the Pacific Northwest coast. *Journal of Geophysical Research: Oceans*, *119*, 2439–2461. https://doi.org/10.1002/2013JC009622

Gill, A. E. (1982). *Atmosphere-ocean dynamics*. Cambridge, MA: Academic Press.

Haidvogel, D. B., Arango, H., Budgell, W. P., Cornuelle, B. D., Curchitser, E., Di Lorenzo, E., ... Wilkin, J. (2008). Ocean forecasting in terrain-following coordinates: Formulation and skill assessment of the Regional Ocean Modeling System. *Journal of Computational Physics*, *227*(7), 3595–3624. https://doi.org/10.1016/j.jcp.2007.06.016

Hall, R. A., & Carter, G. S. (2010). Internal tides in Monterey Submarine Canyon. *Journal of Physical Oceanography*, *41*(1), 186–204. https://doi.org/10.1175/2010JPO4471.1

He, R., & Wilkin, J. L. (2006). Barotropic tides on the southeast New England shelf: A view from a hybrid data assimilative modeling approach. *Journal of Geophysical Research*, *111*, C08002. https://doi.org/10.1029/2005JC003254

Hermann, A. J., Stabeno, P. J., Haidvogel, D. B., & Musgrave, D. L. (2002). A regional tidal/subtidal circulation model of the southeastern Bering Sea: Development, sensitivity analyses and hindcasting. *Deep Sea Research Part II: Topical Studies in Oceanography*, *49*(26), 5945–5967. https://doi.org/10.1016/S0967-0645(02)00328-4

Hinrichsen, H.-H., Dickey-Collas, M., Huret, M., Peck, M. A., & Vikebo, F. B. (2011). Evaluating the suitability of coupled biophysical models for fishery management. *ICES Journal of Marine Science*, *68*(7), 1478–1487. https://doi.org/10.1093/icesjms/fsr056

Hodur, R., Hong, X., Doyle, J., Pullen, J., Cummings, J., Martin, P., & Rennick, M. A. (2002). The Coupled Ocean/Atmosphere Mesoscale Prediction System (COAMPS). *Oceanography*, *15*(1), 88–98. https://doi.org/10.5670/oceanog.2002.39

Holloway, P. E. (2001). A regional model of the semidiurnal internal tide on the Australian North West Shelf. *Journal of Geophysical Research*, *106*(C9), 19625–19638. https://doi.org/10.1029/2000JC000675

Houghton, R. W., & Ho, C. (2001). Diapycnal flow through the Georges Bank Tidal Front: A dye tracer study. *Geophysical Research Letters*, *28*(1), 33–36. https://doi.org/10.1029/2000GL012298

Huthnance, J. M. (1995). Circulation, exchange and water masses at the ocean margin: The role of physical processes at the shelf edge. *Progress in Oceanography*, *35*(4), 353–431. https://doi.org/10.1016/0079-6611(95)80003-C

Huyer, A., Kosro, P. M., Lentz, S. J., & Beardsley, R. C. (1989). Poleward flow in the California current system. In S. J. Neshyba et al. (Eds.), *Poleward flows along eastern ocean boundaries, Coastal and Estuarine Studies* (Vol. 34, pp. 142–159), New York, NY: Springer. https://doi.org/10.1007/978-1-4613-8963-7_12

Janekovic, I., & Powell, B. (2012). Analysis of imposing tidal dynamics to nested numerical models. *Continental Shelf Research*, *34*, 30–40. https://doi.org/10.1016/j.csr.2011.11.017

Johnston, T. M. S., & Merrifield, M. A. (2003). Internal tide scattering at seamounts, ridges, and islands. *Journal of Geophysical Research*, *108*(C6),3180. https://doi.org/10.1029/2002JC001528

Kartadikaria, A. R., Miyazawa, Y., Varlamov, S. M., & Nadaoka, K. (2011). Ocean circulation for the Indonesian seas driven by tides and atmospheric forcings: Comparison to observational data. *Journal of Geophysical Research*, *116*, C09009. https://doi.org/10.1029/2011JC007196

Kelly, S. M., Jones, N. L., Nash, J. D., & Waterhouse, A. F. (2013a). The geography of semidiurnal mode-1 internal-tide energy loss. *Geophysical Research Letters*, *40*, 4689–4693. https://doi.org/10.1002/grl.50872

Kelly, S. M., Jones, N. L., & Nash, J. D. (2013b). A coupled model for Laplace's tidal equations in a fluid with one horizontal dimension and variable depth. *Journal of Physical Oceanography*, *43*(8), 1780–1797. https://doi.org/10.1175/JPO-D-12-0147.1

Kerry, C. G., Powell, B. S., & Carter, G. S. (2014). The impact of subtidal circulation on internal tide generation and propagation in the Philippine Sea. *Journal of Physical Oceanography*, *44*(5), 1386–1405. https://doi.org/10.1175/JPO-D-13-0142.1

Kirincich, A. R., Lentz, S. J., Farrar, J. T., & Ganju, N. K. (2013). The spatial structure of tidal and mean circulation over the inner shelf south of Martha's Vineyard, Massachusetts. *Journal of Physical Oceanography*, *43*(9), 1940–1958. https://doi.org/10.1175/JPO-D-13-020.1

Kumar, N., Feddersen, F., Suanda, S., Uchiyama, Y., & McWilliams, J. (2015). Mid- to inner-shelf coupled ROMS-SWAN model-data comparison of currents and temperature: Diurnal and semidiurnal variability. *Journal of Physical Oceanography*, *46*(3), 841–862. https://doi.org/10.1175/JPO-D-15-0103.1

Kurapov, A. L., Allen, J. S., & Egbert, G. D. (2010). Combined effects of wind-driven upwelling and internal tide on the continental shelf. *Journal of Physical Oceanography*, *40*(4), 737–756. https://doi.org/10.1175/2009JPO4183.1

Lentz, S. J. (1995). Sensitivity of the inner-shelf circulation to the form of the eddy viscosity profile. *Journal of Physical Oceanography*, *25*(1), 19–28.

Lentz, S. J. (2001). The influence of stratification on the wind-driven cross-shelf circulation over the North Carolina Shelf. *Journal of Physical Oceanography*, *31*, 2749–2760.

Lentz, S. J., & Fewings, M. R. (2012). The wind-and wave-driven inner-shelf circulation. *Annual Review of Marine Science*. 4, 317–343.

Lentz, S. J., Fewings, M., Howd, P., Fredericks, J., & Hathaway, K. (2008). Observations and a model of undertow over the inner continental shelf. *Journal of Physical Oceanography*, *38*, 2341–2357.

Lerczak, J. A., Winant, C. D., & Hendershott, M. C. (2003). Observations of the semidiurnal internal tide on the southern California slope and shelf. *Journal of Geophysical Research*, *108*(C3), 3068. https://doi.org/10.1029/2001JC001128

Liu, Y., MacCready, P., Hickey, B. M., Dever, E. P., Kosro, P. M., & Banas, N. S. (2009). Evaluation of a coastal ocean circulation model for the Columbia River plume in summer 2004. *Journal of Geophysical Research*, *114*, C00B04. https://doi.org/10.1029/2008JC004929

MacKinnon, J. A., & Gregg, M. C. (2003a). Mixing on the late-summer New England Shelf-Solibores, shear, and stratification. *Journal of Physical Oceanography*, *33*(7), 1476–1492.

MacKinnon, J. A., & Gregg, M. C. (2003b). Shear and baroclinic energy flux on the summer New England shelf. *Journal of Physical Oceanography*, *33*(7), 1462–1475.

Marchesiello, P., McWilliams, J. C., & Shchepetkin, A. (2001). Open boundary conditions for long-term integration of regional oceanic models. *Ocean Modelling*, *3*(1), 1–20.

Mark, D. J., Spargo, E. A., Westerink, J. J., & Luettich, R. A. (2004). *ENPAC 2003: A tidal constituent database for eastern North Pacific Ocean* (Tech. Rep. ERDC/CHL-TR-04–12). Washington, DC: Coastal and Hydraulics Laboratory, U.S. Army Corps of Engineering.

Mason, E., Molemaker, J., Shchepetkin, A. F., Colas, F., McWilliams, J. C., & Sangra, P. (2010). Procedures for offline grid nesting in regional ocean models. *Ocean Modelling*, *35*(12), 1–15. https://doi.org/10.1016/j.ocemod.2010.05.007

McPhee-Shaw, E. E., Siegel, D. A., Washburn, L., Brzezinski, M. A., Jones, J. L., Leydecker, A., & Melack, J. (2007). Mechanisms for nutrient delivery to the inner shelf: Observations from the Santa Barbara Channel. *Limnology and Oceanography*, *52*(5), 1748–1766.

Melton, C., Washburn, L., & Gotschalk, C. (2009). Wind relaxations and poleward flow events in a coastal upwelling system on the central California coast. *Journal of Geophysical Research*, *114*, C11016. https://doi.org/10.1029/2009JC005397

Mitarai, S., Siegel, D. A., Watson, J. R., Dong, C., & McWilliams, J. C. (2009). Quantifying connectivity in the coastal ocean with application to the Southern California Bight. *Journal of Geophysical Research*, *114*, C10026. https://doi.org/10.1029/2008JC005166

Morgan, S. G., Fisher, J. L., Mace, A. J., Akins, L., Slaughter, A. M., & Bollens, S. M. (2009a). Cross-shelf distributions and recruitment of crab postlarvae in a region of strong upwelling, *Marine Ecology Progress Series*, *380*, 173–185.

Morgan, S. G., Fisher, J. L., Miller, S. H., McAfee, S. T., & Largier, J. L. (2009b). Nearshore larval retention in a region of strong upwelling and recruitment limitation. *Ecology*, *90*(12), 3489–3502.

Munk, W., & Wunsch, C. (1998). Abyssal recipes II: Energetics of tidal and wind mixing. *Deep Sea Research Part I: Oceanographic Research Papers*, *45*(12), 1977–2010. https://doi.org/10.1016/S0967-0637(98)00070-3

Nam, S., & Send, U. (2011). Direct evidence of deep water intrusions onto the continental shelf via surging internal tides. *Journal of Geophysical Research*, *116*, C05004. https://doi.org/10.1029/2010JC006692

Osborne, J. J., Kurapov, A. L., Egbert, G. D., & Kosro, P. M. (2011). Spatial and temporal variability of the M 2 internal tide generation and propagation on the Oregon shelf. *Journal of Physical Oceanography*, *41*(11), 2037–2062.

Osborne, J. J., Kurapov, A. L., Egbert, G. D., & Kosro, P. M. (2014). Intensified diurnal tides along the Oregon Coast. *Journal of Physical Oceanography*, *44*(7), 1689–1703. https://doi.org/10.1175/JPO-D-13-0247.1

Pawlowicz, R., Beardsley, B., & Lentz, S. (2002). Classical tidal harmonic analysis including error estimates in MATLAB using T-TIDE. *Computers & Geosciences*, *28*(8), 929–937. https://doi.org/10.1016/S0098-3004(02)00013-4

Pidgeon, E. J., & Winant, C. D. (2005). Diurnal variability in currents and temperature on the continental shelf between central and southern California. *Journal of Geophysical Research*, *110*, C03024. https://doi.org/10.1029/2004JC002321

Ponte, A. L., & Cornuelle, B. D. (2013). Coastal numerical modelling of tides: Sensitivity to domain size and remotely generated internal tide. *Ocean Modelling*, *62*, 17–26. https://doi.org/10.1016/j.ocemod.2012.11.007

Queiroga, H., & Blanton, J. (2004). Interactions between behaviour and physical forcing in the control of horizontal transport of decapod crustacean larvae. *Advances in Marine Biology*, *47*, 107–214. https://doi.org/10.1016/S0065-2881(04)47002-3

Roughan, M., Terrill, E. J., Largier, J. L., & Otero, M. P. (2005). Observations of divergence and upwelling around Point Loma, California. *Journal of Geophysical Research*, *110*, C04011. https://doi.org/10.1029/2004JC002662

Shchepetkin, A. F., & McWilliams, J. C. (2005). The regional oceanic modeling system (ROMS): A split-explicit, free-surface, topography-following-coordinate oceanic model. *Ocean Modelling*, *9*(4), 347–404. https://doi.org/10.1016/j.ocemod.2004.08.002

Shchepetkin, A. F., & McWilliams, J. C. (2009). Correction and commentary for 'Ocean forecasting in terrain-following coordinates: Formulation and skill assessment of the regional ocean modeling system' by Haidvogel et al., J. Comp. Phys. 227, pp. 3595–3624. *Journal of Computational Physics*, *228*(24), 8985–9000. https://doi.org/10.1016/j.jcp.2009.09.002

Simpson, J. H., & Hunter, J. R. (1974). Fronts in the Irish Sea. *Nature*, *250*(5465), 404–406. https://doi.org/10.1038/250404a0

Suanda, S. H., & Barth, J. A. (2015). Semidiurnal baroclinic tides on the central oregon inner shelf. *Journal of Physical Oceanography*, *45*(10), 2640–2659. https://doi.org/10.1175/JPO-D-14-0198.1

Suanda, S. H., Kumar, N., Miller, A. J., Di Lorenzo, E., Haas, K., Cai, D., Edwards, C. A., . . . Feddersen, F. (2016). Wind relaxation and a coastal buoyant plume north of Pt. Conception, CA: Observations, simulations, and scalings. *Journal of Geophysical Research: Oceans, 121*, 7455–7475. https://doi.org/10.1002/2016JC011919

Tapia, F. J., Navarrete, S. A., Castillo, M., Menge, B. A., Castilla, J. C., Largier, J., . . . Barth, J. A. (2009). Thermal indices of upwelling effects on inner-shelf habitats. *Progress in Oceanography*, *83*(1–4), 278–287. https://doi.org/10.1016/j.pocean.2009.07.035

Thorpe, S. A. (1999). The generation of alongslope currents by breaking internal waves. *Journal of Physical Oceanography*, *29*(1), 29–38.

Thyng, K. M., Greene, C. A., Hetland, R. D., Zimmerle, H. M., & DiMarco, S. F. (2016). True colors of oceanography: Guidelines for effective and accurate colormap selection. *Oceanography*, *29*(3), 9–13.

Tilburg, C. E., & Garvine, R. W. (2003). Three-dimensional flow in a shallow coastal upwelling zone: Alongshore convergence and divergence on the New Jersey Shelf. *Journal of Physical Oceanography*, *33*(10), 2113–2125. https://doi.org/10.1175/1520-0485(2003)033

Umlauf, L., & Burchard, H. (2003). A generic length-scale equation for geophysical turbulence models. *Journal of Marine Research*, *61*(2), 235–265.

Veneziani, M., Edwards, C. A., Doyle, J. D., & Foley, D. (2009). A central California coastal ocean modeling study: 1. Forward model and the influence of realistic versus climatological forcing. *Journal of Geophysical Research*, *114*, C04015. https://doi.org/10.1029/2008JC004774

Vitousek, S., & Fringer, O. B. (2011). Physical vs. numerical dispersion in nonhydrostatic ocean modeling. *Ocean Modelling*, *40*(1), 72–86. https://doi.org/10.1016/j.ocemod.2011.07.002

Walter, R. K., Reid, E. C., Davis, K. A., Armenta, K. J., Merhoff, K., & Nidzieko, N. J. (2017). Local diurnal wind-driven variability and upwelling in a small coastal embayment. *Journal of Geophysical Research: Oceans*, *122*, 955–972. https://doi.org/10.1002/2016JC012466

Walter, R. K., Woodson, C. B., Arthur, R. S., Fringer, O. B., & Monismith, S. G. (2012). Nearshore internal bores and turbulent mixing in southern Monterey Bay. *Journal of Geophysical Research*, *117*, C07017. https://doi.org/10.1029/2012JC008115

Warner, J. C., Armstrong, B., He, R., & Zambon, J. B. (2010). Development of a Coupled Ocean-Atmosphere-Wave-Sediment Transport (COAWST) modeling system. *Ocean Modelling*, *35*(3), 230–244. https://doi.org/10.1016/j.ocemod.2010.07.010

Warner, J. C., Sherwood, C. R., Arango, H. G., & Signell, R. P. (2005). Performance of four turbulence closure models implemented using a generic length scale method. *Ocean Modelling*, *8*(1–2), 81–113. https://doi.org/16/j.ocemod.2003.12.003

Washburn, L., Fewings, M. R., Melton, C., & Gotschalk, C. (2011). The propagating response of coastal circulation due to wind relaxations along the central California coast. *Journal of Geophysical Research*, *116*, C12028. https://doi.org/10.1029/2011JC007502

Waterhouse, A. F., MacKinnon, J. A., Nash, J. D., Alford, M. H., Kunze, E., Simmons, H. L., . . . Lee, C. M. (2014). Global patterns of diapycnal mixing from measurements of the turbulent dissipation rate. *Journal of Physical Oceanography*, *44*(7), 1854–1872. https://doi.org/10.1175/JPO-D-13-0104.1

Wijesekera, H. W., Allen, J. S., & Newberger, P. A. (2003). Modeling study of turbulent mixing over the continental shelf: Comparison of turbulent closure schemes. *Journal of Geophysical Research*, *108*(C3), 3103. https://doi.org/10.1029/2001JC001234

Winant, C. D. (2006). Three-dimensional wind-driven coastal circulation past a headland. *Journal of Physical Oceanography*, *36*(7), 1430–1438. https://doi.org/10.1175/JPO2915.1